iScience

CellPress
OPEN ACCESS

Article

Semi-supervised analysis of myeloid and T cell behavior in *ex vivo* ovarian tumor slices reveals changes in cell motility after treatments

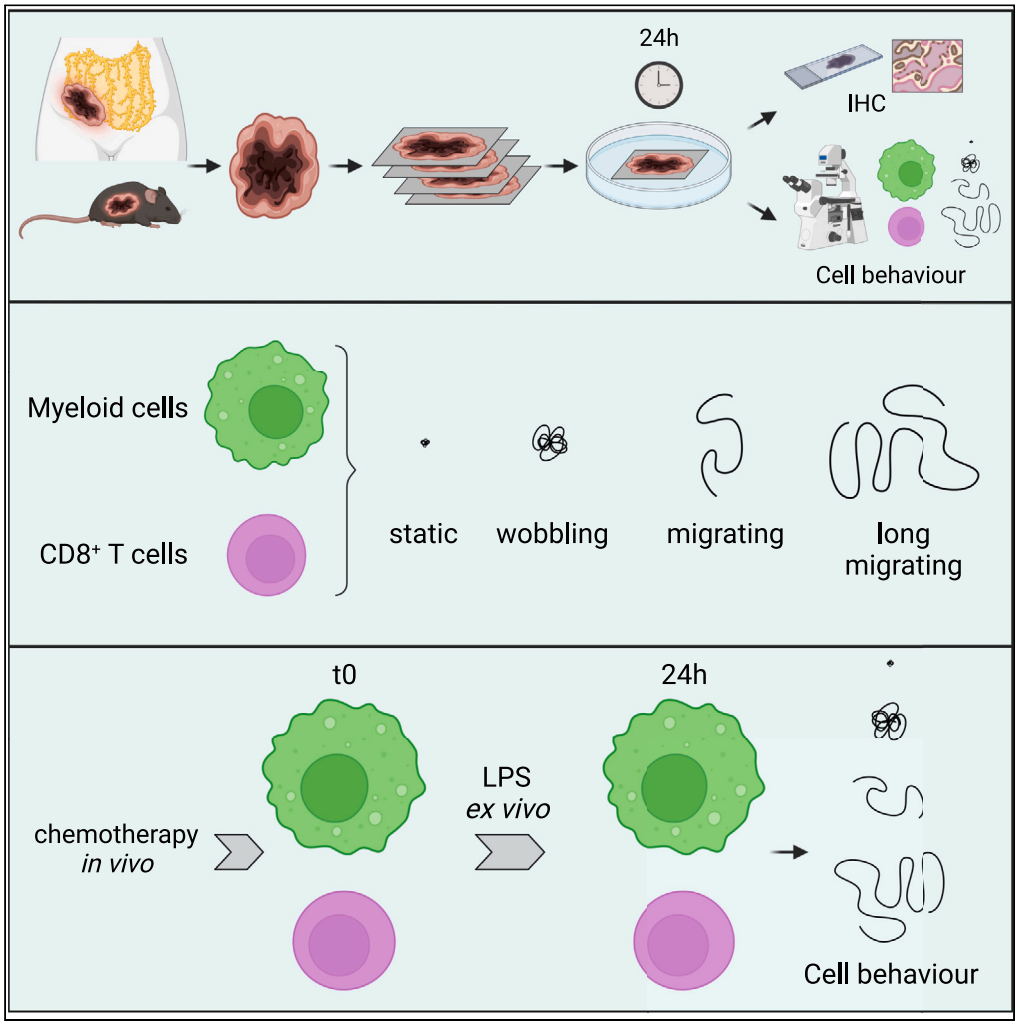

Florian Laforêts, Panoraia Kotantaki, Beatrice Malacrida, Samar Elorbany, Ranjit Manchanda, Emmanuel Donnadieu, Frances Balkwill

f.balkwill@qmul.ac.uk

Highlights

Human and mouse ovarian cancer slices used to model treatments *ex vivo*

CD8⁺ T and myeloid cells display four different behaviors *ex vivo*

CD8⁺ T and myeloid cell behavior stable for 24h and altered by lipopolysaccharide (LPS) *ex vivo*

In vivo chemotherapy leads to reduced CD8⁺ T and myeloid cell motility *ex vivo*

Laforêts et al., iScience *26*, 106514
April 21, 2023
https://doi.org/10.1016/j.isci.2023.106514

iScience

CellPress
OPEN ACCESS

Article

Semi-supervised analysis of myeloid and T cell behavior in *ex vivo* ovarian tumor slices reveals changes in cell motility after treatments

Florian Laforêts,[1] Panoraia Kotantaki,[1] Beatrice Malacrida,[1] Samar Elorbany,[1] Ranjit Manchanda,[2,3,4] Emmanuel Donnadieu,[5,6] and Frances Balkwill[1,6,7,*]

SUMMARY

Studies of the high-grade serous ovarian cancer (HGSOC) tumor microenvironment, the most lethal gynecological cancer, aim to enhance the efficiency of established therapies. Cell motility is an important process of anti-tumor response. Using *ex vivo* human and mouse HGSOC tumor slices combined with time-lapse imaging, we assessed the motility of CD8$^+$ T and myeloid cells. We developed a semi-supervised analysis of cell movements, identifying four cell behaviors: migrating, long migrating, static, and wobbling. Tumor slices were maintained 24h *ex vivo*, retaining viability and cell movements. *Ex vivo* treatments with lipopolysaccharide altered CD8$^+$ T and myeloid cell behavior. *In vivo* chemotherapy reduced *ex vivo* cell movements in human and mouse tumors and differentially affected CD8$^+$ T and myeloid cells in chemo-sensitive and chemo-resistant mouse models. *Ex vivo* tumor slices can extend *in vivo* mouse studies to human, providing a stepping stone to translate mouse cancer studies to clinical trials.

INTRODUCTION

The growth, progression, and dissemination of human tumors are driven by a complex cooperation between malignant cells, corrupted host cells, and an ensemble of extracellular factors.[1] Studies of this tumor microenvironment (TME) have led to discoveries of new cancer therapies.[2,3]

High-grade serous ovarian cancer (HGSOC) is the most common and deadly type of ovarian cancer.[4,5] Fewer than 35% of patients survive beyond five years after diagnosis.[6] There is, therefore, need to better understand the HGSOC TME in order to improve therapy efficiency and prevent relapse.

Studies of its cellular and extracellular composition[7,8] along with its response to therapies, particularly the role of the host's immune response, have led to a better understanding of the HGSOC TME. Our group has recently developed new models to study this TME: mouse syngeneic models[9] and *in vitro* multi-cellular models.[10,11] We used these models to demonstrate the impact of chemotherapy on the innate and adaptive immune responses[12–14] and investigated the role and therapeutic potential of anti-interleukin 6 (anti-IL-6).[15,16] Such studies combine an array of techniques: transcriptomics, proteomics, histology, and flow cytometry, which together provide insights into the TME and its response to various therapies. However, these approaches are limited to providing a fixed, albeit detailed image of the TME and omit its dynamic nature. Furthermore, although *in vitro* multi-cellular models provide a useful human cell pre-clinical model, they do not recapitulate the whole human TME. More human models and dynamic approaches are needed to complement our existing tools.

The *ex vivo* tumor slice assay allows the study of a live tumor and its response to various treatments.[17,18] Combined with time-lapse imaging, the *ex vivo* tissue slice assay enables the monitoring of resident immune cells in real-time, including in ovarian carcinomas.[19,20] This approach has shed light on the migration of CD8$^+$ T cells and the involvement of the extracellular matrix (ECM) and tumor-associated macrophages in restricting their movements and impeding them from contacting tumor cells.[21] The migration of T cells has emerged as an important parameter to take into account their anti-tumor function, as it enables lymphocytes to interact with antigen-presenting cells as well as malignant cells. Thus, monitoring T cell motility in an intact human TME, identifying obstacles, and designing strategies to overcome them represent

[1]Barts Cancer Institute, Queen Mary University of London, Charterhouse Square, EC1M6BQ London, UK

[2]Wolfson Institute of Population Health, CRUK Barts Cancer Centre, Queen Mary University of London, EC1M 6BQ London, UK

[3]Department of Gynaecological Oncology, Barts Health NHS Trust, Royal London Hospital, E1 1BB London, UK

[4]Department of Health Services Research and Policy, London School of Hygiene & Tropical Medicine, WC1H 9SH London, UK

[5]Université Paris Cité, CNRS, INSERM, Equipe Labellisée Ligue Contre le Cancer, Institut Cochin, 75014 Paris, France

[6]These authors contributed equally

[7]Lead contact

*Correspondence: f.balkwill@qmul.ac.uk

https://doi.org/10.1016/j.isci.2023.106514

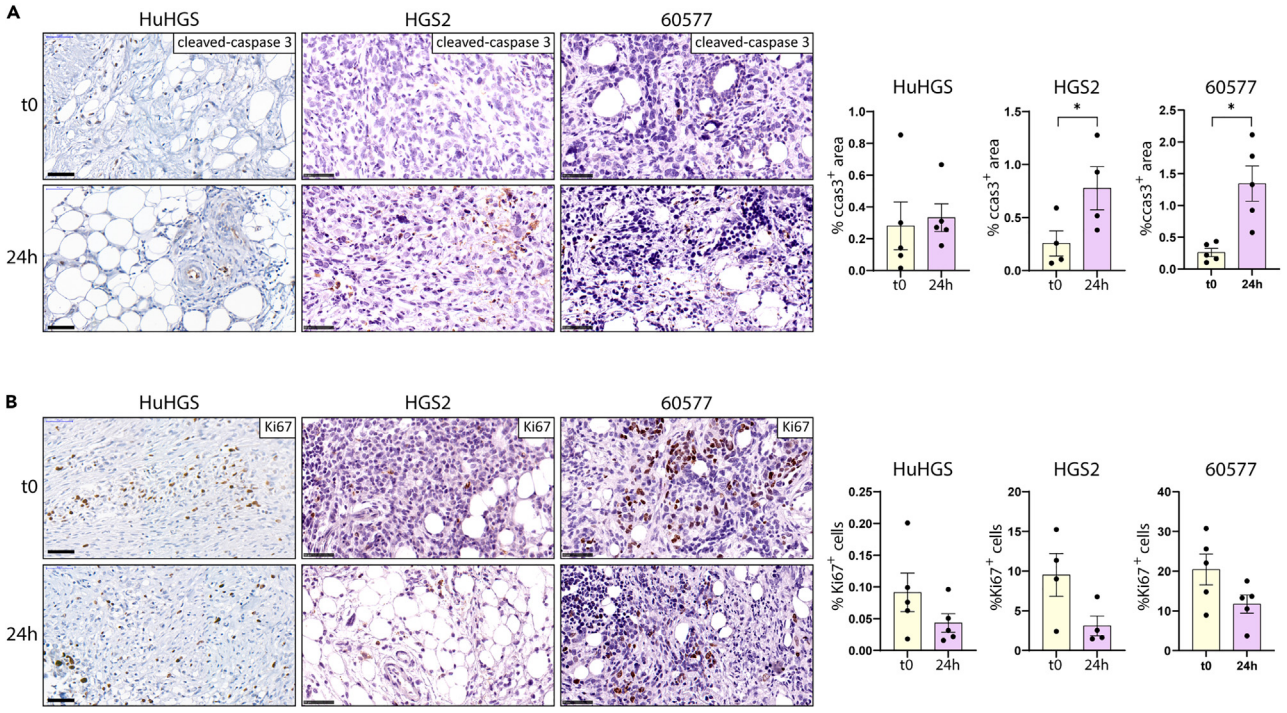

Figure 1. Human and mouse high-grade serous tumor slices are viable *ex vivo* for 24h

Immunohistochemistry of human HGSOC (HuHGS), mouse HGS2 and 60577 tumor slices fixed either immediately after slicing (t0) or put in culture for 24h, and analyzed for (A) apoptosis with cleaved caspase-3 (ccas3) and (B) proliferation with Ki67. The left panels show representative images of IHC. The right panels show the staining quantifications. ccas3, the % positively stained area was quantified; Ki67, the % positively stained cells was quantified. Scale bars, 50 μm. Each dot represents the average quantification of the staining of 1–5 different slices of the same tumor at a given time point. Histograms show the mean ± SEM. Number of tumors for each model: human, 5; HGS2, 4; 60577, 5. Paired t test, *p < 0.05.

important aspects of cancer immunotherapy research. Studies have so far focused on $CD8^+$ T cells, and migration in *ex vivo* tumor slices has only been studied for periods of a few hours after slicing.[19,20] Developing the tumor slice assay, by investigating the behavior of other cell types and maintaining the slices long enough in culture to assess the effect of treatments, would enable the study of new therapies on cell behavior and could shed further light on the dynamic functioning of the HGSOC TME.

Here, we report for the first time the characterization of the movements of myeloid cells *ex vivo*, in addition to further studies on $CD8^+$ T cells. We assessed their behavior, including after 24h *ex vivo*, in human HGSOC biopsy tissue slices (HuHGS) and two mouse HGSOC models, enabling us to study cell movement in response to *ex vivo* treatments. We developed a semi-supervised approach that provides an in-depth characterization of cell behavior, by distinguishing different types of cellular movements. Finally, we show the effect of LPS *ex vivo* and chemotherapy *in vivo* treatments on the behavior of $CD8^+$ T and myeloid cells, assessing the dynamic response of those cell types to therapy. When developing new therapies, this approach enables to expand results obtained *in vivo* in mice to *ex vivo* in human samples, providing a platform to translate mouse experimental results to clinical trials.

RESULTS

Human and mouse high-grade serous ovarian tumor slices are stable over 24 h *ex vivo*

We first assessed the *ex vivo* viability of the tumor slices over 24 h. Samples were obtained from human HGSOC omental tumors (HuHGS) and from tumor-bearing omentum from the mouse HGSOC models, HGS2 and 60577.[9] Samples were cut into 350 μm slices, cultured *ex vivo* in medium optimized for slice viability and either fixed immediately (t0) or after 24h, embedded in paraffin and longitudinally sectioned for immunohistochemistry (IHC). We performed IHC for cleaved caspase-3 (ccas3) and Ki67 to assess apoptosis and proliferation, respectively (Figure 1). The apoptosis levels were stable over 24h in human tumors and showed a low but significant increase of 0.5–1% cells in HGS2 and 60577 mouse tumors

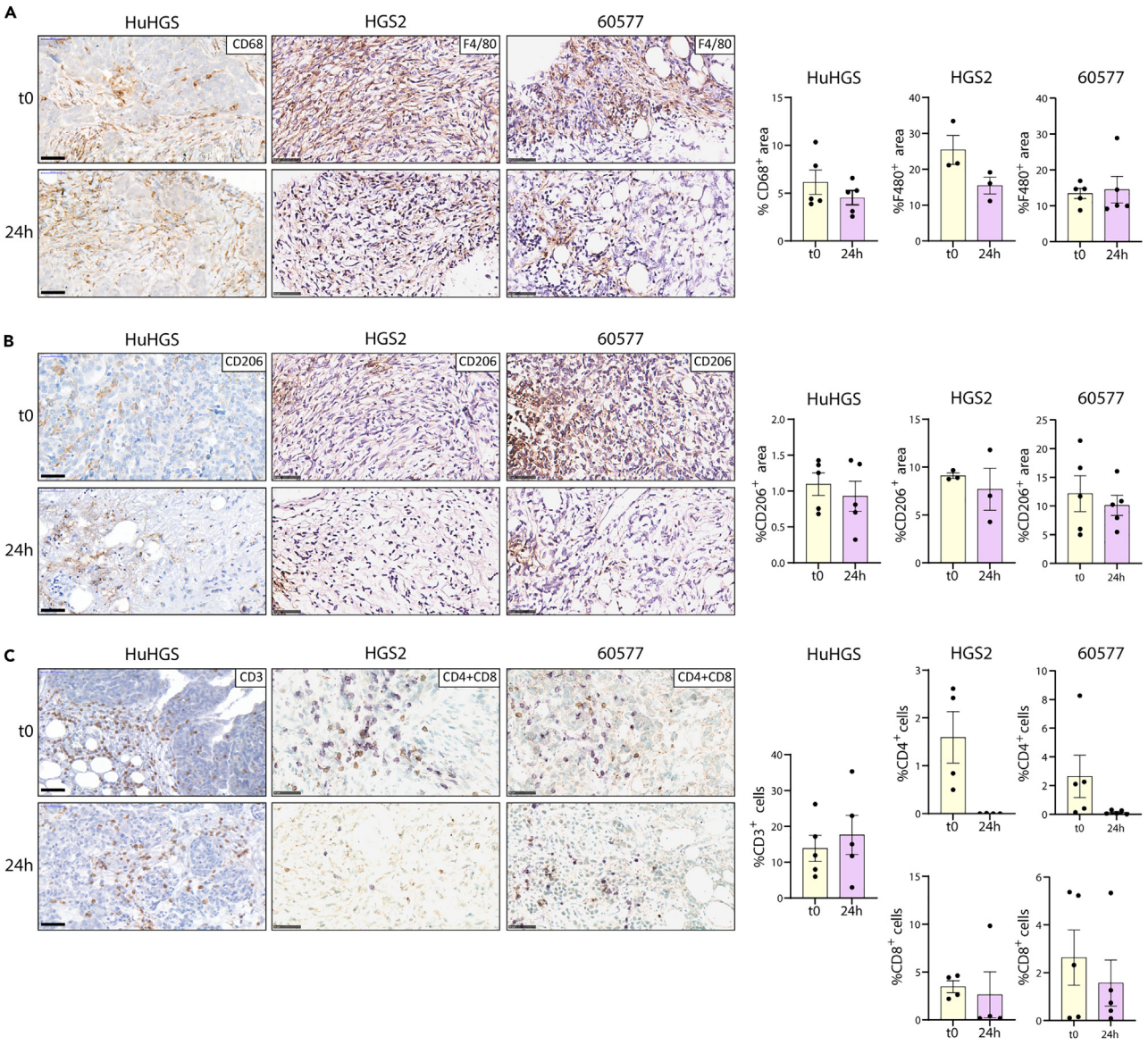

Figure 2. Stability of the myeloid cell and T cell content of human and mouse high-grade serous tumor slices *ex vivo* over 24h

(A–C) IHC of human HGSOC (HuHGS), mouse HGS2 and 60577 tumor slices fixed either immediately after slicing (t0) or put in culture for 24h, and analyzed for (A), myeloid cells with CD68 in human and F4/80 in HGS2 and 60577 in brown; (B) M2-polarized myeloid cells with CD206 in brown; (C) T cells with CD3 in human (brown) and a CD4/CD8 dual staining in HGS2 and 60577 (CD4, purple; CD8, brown). (A–C) the left panels show representative images of IHC. The right panels show the staining quantifications. For CD68 and CD206, the % positively stained area was quantified; whereas for CD3, CD4, and CD8, the % positively stained cells was quantified. Scale bars, 50 μm. Stainings were quantified over 1 to 5 different slices of the same tumor. Number of tumors for each model: human, 5; HGS2, 4; 60577, 5. Histograms show the mean ± SEM. Paired t test, all p values between t0 and 24h were >0.05.

(Figure 1A). No significant difference in the proportion of Ki67$^+$ cells was observed between t0 and 24h in the human and mouse tumor slices (Figure 1B).

To further assess the stability of HGSOC tumor slices *ex vivo*, we measured myeloid and T cell number using IHC (Figure 2). There was no change in CD68$^+$ cells in human and F4/80$^+$ cells in mouse tumor slices over 24h (Figure 2A). CD206 staining was also unchanged (Figure 2B), suggesting the myeloid cell population was stable *ex vivo* over 24h both in numbers and in macrophage polarity. Numbers of CD3$^+$ T cells did not vary between t0 and 24h in human tumors (Figure 2C). In HGS2 and 60577 tumor slices however, there was a marked decrease in CD4$^+$ and to a lesser extent CD8$^+$ T cells.

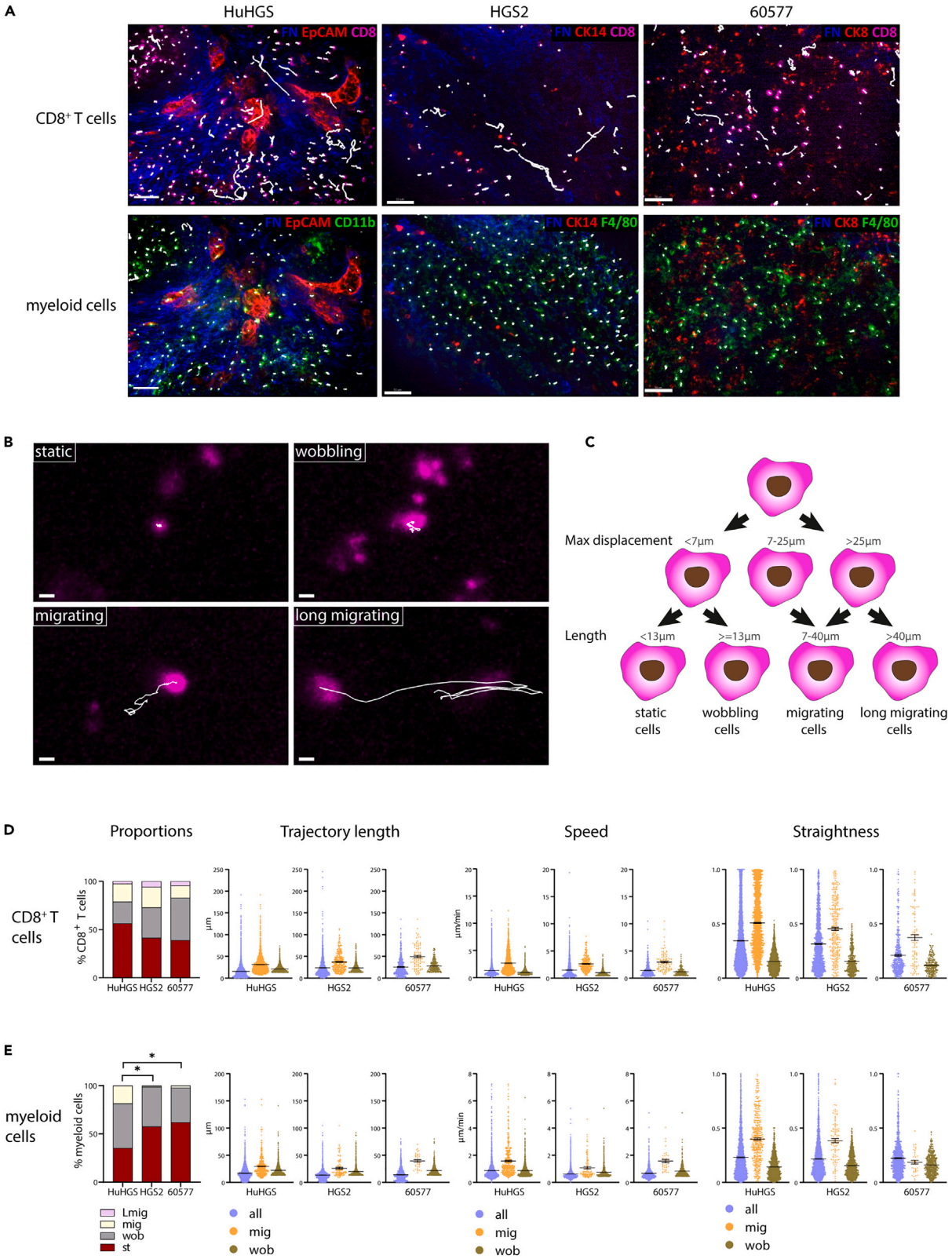
A
HuHGS
HGS2
60577
CD8⁺ T cells
myeloid cells
FN EpCAM CD8
FN CK14 CD8
FN CK8 CD8
FN EpCAM CD11b
FN CK14 F4/80
FN CK8 F4/80
B
static
wobbling
migrating
long migrating
C
Max displacement
<7µm
7-25µm
>25µm
Length
<13µm
>=13µm
7-40µm
>40µm
static cells
wobbling cells
migrating cells
long migrating cells
D
Proportions
Trajectory length
Speed
Straightness
CD8⁺ T cells
% CD8⁺ T cells
µm
µm/min
HuHGS HGS2 60577
E
myeloid cells
% myeloid cells
Lmig
mig
wob
st
all
mig
wob

Figure 3. Characterizing the behavior of immune cells *ex vivo* in the tumor microenvironment of human and mouse high grade serous ovarian tumor slices

(A) live slices obtained from human HGSOC, HGS2, and 60577 tumors were stained for: fibronectin (blue), myeloid cells (green; human, CD11b; mouse, F4/80); malignant cells (red; Human, EpCAM; HGS2, cytokeratin 14; 60577, cytokeratin 8); $CD8^+$ T cells (pink) and imaged in real-time. Tracks of $CD8^+$ T cells (top panel) and myeloid cells (bottom panel) are shown in white. Different types of trajectories are visible both for T cells and myeloid cells in human (HuHGS), HGS2, and 60577. Scale bars 50 μm.

(B) Images showing tracks (white) of individual cells (CD8, pink) representative of four distinct types of behavior: static, wobbling, migrating, and long migrating. Scale bars 8 μm.

(C) Strategy for behavioral categorization: $CD8^+$ T cells and myeloid cell trajectories are split into four types of behavior using migration metrics: maximum displacement and trajectory length. Cells with maximum displacement < 7um and trajectory length <13 μm are considered static, cells with maximum displacement < 7um and trajectory length >13 μm are considered wobbling, cells with maximum displacement 7-25um and trajectory length 7-40um are considered migrating and cells with maximum displacement >25um and trajectory length >40 μm are considered long migrating.

(D and E) Proportions of the different types of behavior (red, static; gray, wobbling; yellow, migrating; pink long migrating), trajectory length, mean speed and trajectory straightness for the different behavior categories (purple, all, all cells; orange, mig, migrating, and long migrating cells together; khaki, wob, wobbling cells) for (D) $CD8^+$ T cells and (E) myeloid cells (human, $CD11b^+$ cells; HGS2 and 60577, $F4/80^+$ cells) in human HGSOC (HuHGS), HGS2 and 60577 mouse tumors. Histograms show the mean ± SEM. Number of tumors/$CD8^+$ T cells/myeloid cells for each model: human, 5/12068/2976; HGS2, 9/1800/3303; 60577, 5/476/1215.

Overall, these results show a relatively stable TME *ex vivo* in terms of viability and myeloid cell populations in human and mouse tumor slices over 24h, with a stable T cell population in human and a declining population of $CD4^+$ T cells in mouse tumor slices.

$CD8^+$ T and myeloid cell display four distinguishable dynamic behavior types in human and mouse *ex vivo* high grade serous ovarian cancer tumor slices

To characterize the dynamic behavior of $CD8^+$ T and myeloid cells in HuHGS, HGS2, and 60577 slices *ex vivo*, we performed time-lapse experiments on live tumor slices labeled with directly conjugated fluorescent antibodies, according to a previously published method.[19] Confocal microscopy and fluorescent time-lapse imaging allowed us to monitor the movements of resident immune cells in real-time during a 30 min recording. In addition to myeloid cells (green; CD11b in HuHGS, F4/80 in HGS2 and 60577) and $CD8^+$ T cells (pink), we stained malignant cells (red; EpCAM in HuHGS, CK14 in HGS2, and CK8 in 60577) and fibronectin (blue; FN1) as a component of the stromal ECM (Figure 3A, Videos S1, S2, and S3). HuHGS slices had clusters of $EpCAM^+$ malignant cells easily distinguishable from the stroma which was revealed by the FN1 staining. $CD8^+$ T cells were largely located in the stroma, as reported previously,[21] and rarely penetrated the malignant cell islets. CD11b staining was mutually exclusive with EpCAM showing that myeloid cells were also located outside malignant cell islets (Figure 3A). This separation between stroma and malignant cell areas was less marked in HGS2 and 60577 tumors (Figure 3A), as the malignant cells were more dispersed in the TME. However, we observed few contacts between $CD8^+$ T cell and malignant cells in HGS2 and 60577 tumor slices.

Our observations of cell movements led us to distinguish different types of behavior. In all three tumor types, we observed that a large proportion of both cell types were static over a 30 min time course (Figure 3B and Video S4). A small portion of cells, especially CD8 T cells, displayed migration (Figure 3B and Video S5) while another group displayed little or no displacement but were still motile (Figure 3B and Video S6). Those movements, either non-directional migration or cytoplasmic extensions, resulted in a "wobbling" motion, distinct from both directional migration and static cells. Therefore, instead of simply quantifying migration, we decided to take the wobbling population into account. In addition, some $CD8^+$ T cells migrated over relatively long distances (Figure 3B and Video S7) in all three tumor types. Therefore, we decided to distinguish between migrating and long migrating cells. As a result, we identified four different types of cell behavior: static, wobbling, migrating, and long migrating (Figure 3B).

Analyses of myeloid and T cell movements

To distinguish between those four populations we tracked the movements of individual cells with the software Imaris (Bitplane) and extracted movement metrics for each cell trajectory. We developed a semi-supervised approach, with empirically determined thresholds based on two movement metrics: the maximum displacement (distance between a cell's initial position and the furthest it has moved from it - MaxDis) and the trajectory length. The MaxDis splits migrating from non-migrating cells and the trajectory length splits static from wobbling and migrating from long migrating cells, respectively (Figure 3C). Our observations and previous studies[22] show that $CD8^+$ T cells can display a back and forth migration pattern.

The standard displacement is the distance between a cell's initial and last positions. Therefore, we used the MaxDis rather than the standard displacement classifying the cells that migrated back to their initial position as non-migrating cells (Figure 3C).

To semi-automate this analysis we established a pipeline in R. This aggregated all movement metrics of interest, computed the maximum displacement of all cells for all time-lapse experiments, merged the cell populations of two duplicate time-lapse movies and distinguished the static, wobbling, migrating, and long migrating cell populations from each other. The script produced.csv outputs to plot each metric of interest and calculated the proportions of cells belonging to each behavior category.

We used this behavior category approach to characterize the movements of $CD8^+$ T and myeloid cells in freshly established HuHGS, HGS2 and 60577 tumor slices. All three tumor types had similar proportions for $CD8^+$ T cell behavior: 40–60% static, 20–40% wobbling, 15–20% migrating, and 2–10% long migrating (Figures 3D and S1A). They also had similar mean trajectory length (15-25 μm), mean speed (1.3–1.5 μm/min), and mean straightness of trajectory (0.21–0.31) (Figure 3D). We then compared the movements of the migrating and wobbling sub-groups of $CD8^+$ T cells. The migrating $CD8^+$ T cells (encompassing migrating plus long migrating populations) in both mouse and human tumor slices moved twice as far and twice as fast than the wobbling cells. As expected, migrating cells had a more linear trajectory (Figure 3D).

On average, myeloid cells migrated much less than $CD8^+$ T cells. The proportion of myeloid cells that wobbled was similar in HuHGS, HGS2 and 60577 tumor slices (Figures 3E and S1B). However, there were significantly more migrating (18.37%) and less static (35.24%) myeloid cells in HuHGS than in HGS2 and 60577 slices (migrating, 1.32% and 2.26%; static, 57.50% and 61.88%, respectively, in % of the control mean (Figures 3E and S1B). Consistent with differences in migrating proportions, human myeloid cells moved faster (0.87 μm/min) than in the mouse models (0.61 μm/min in HGS2 and 0.67 μm/min in 60577), although straightness of trajectory was similar in all three tumor types. Similar to $CD8^+$ T cells, the migrating myeloid cells moved faster, further and more directionally than the wobbling myeloid cells (Figure 3E).

These results show that we can identify and quantify the movements of different types of $CD8^+$ T and myeloid cell behavior and that those cells display similar behavior in human and mouse *ex vivo* tumor slices. In addition, we can further characterize which behavior-specific sub-group contributes to the movements observed in the overall populations.

$CD8^+$ T and myeloid cells behavior maintain their behavior *ex vivo* for 24h in mouse and human high grade serous ovarian cancer tumor slices

We next assessed the stability of $CD8^+$ T and myeloid cell behavior over 24h monitoring HuHGS, HGS2, and 60577 tumor slices shortly after slicing (t0) and 24h later (Figures 4A, 4B, S2A, and S2B).

Trajectory length of $CD8^+$ T cells significantly increased in human (+36.1%) and decreased in HGS2 (−26.7%) and 60577 (−48.9%) after 24h (Figure 4C). There was also a significant decrease of speed and trajectory straightness in HuHGS and both mouse models (Figure 4C). The decrease in speed at 24h was more pronounced in the mouse models (HGS2 -41.3%; 60577–56.9%) than in human (−5.5%), suggesting human $CD8^+$ T cells are more stable. To determine what sub-group of $CD8^+$ T cell contributes to these changes, we also analyzed the proportion of different cell behaviors and quantified their movements. After 24h, $CD8^+$ T cells displayed the four types of behavior categories previously observed at t0 (Figures 4C and S2C). In HuHGS and 60577, the proportions for all four categories of behavior were maintained at 24h compared to t0 (Figures 4C and S2C). In HGS2 however, while static, wobbling and long migrating proportions were stable, there was a significant decrease in the proportion of migrating $CD8^+$ T cells (Figures 4C and S2C). The analysis of behavior-specific sub-populations (wobbling and migrating) showed the small increase in movements observed at 24h in HuHGS is likely due to an increase in both wobbling and migrating cell movements (Figure S3A). The increase in migrating $CD8^+$ T cells trajectory length and speed in HGS2 (respectively +58.6% and +39.0%), not observed in wobbling cells, suggests the global reduction in $CD8^+$ T cells movement observed in this model is due to a decrease in the number of migrating cells, not to a change in migrating cell behavior (Figure S3A).

There was a small increase in myeloid cell trajectory length and speed in HuHGS (respectively +5.4% and +18.3%) but no change in behavior at 24h in the HGS2 and 60577 tumor slices, apart from a significant

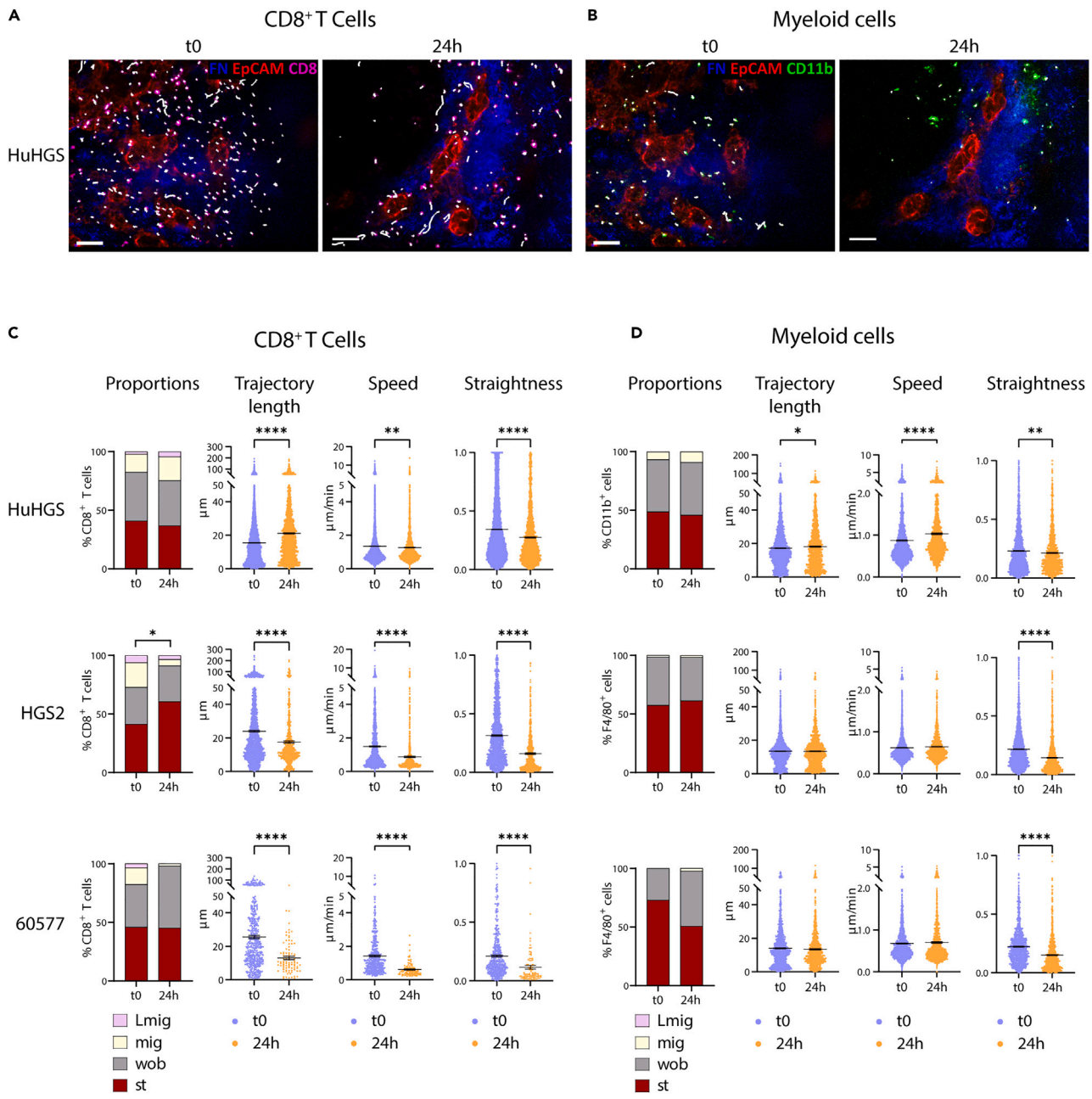

Figure 4. Stability of CD8$^+$ T and myeloid cell behavior over 24h *ex vivo* in human and mouse tumor slices

(A and B) Live human HGSOC tumor slices were stained for: fibronectin (blue), myeloid cells (green, CD11b), malignant cells (red, EpCAM) and CD8$^+$ T cells (pink) and imaged in real-time either shortly after slicing or after 24h *ex vivo*. Tracks of CD8$^+$ T cells, (A), and myeloid cells, (B), are shown in white. Scale bars 50 µm.

(C and D) Proportions of the different types of behavior (red, st, static; gray, wob, wobbling; yellow, mig, migrating; pink, Lmig, long migrating), trajectory length, mean speed and trajectory straightness shortly after slicing (t0, purple) and after 24h *ex* vivo (24h, orange) for (C), CD8$^+$ T cells and (D), myeloid cells (human, CD11b$^+$ cells; HGS2 and 60577, F4/80$^+$ cells) in human HGSOC (HuHGS), HGS2 and 60577 tumors. Histograms display the mean ± SEM. Number of tumors/CD8$^+$ T cells/myeloid cells for each model and condition: human, t0 9/12068/2976, 24h 9/2410/1558; HGS2, t0 9/1800/3303, 24h 9/731/1616; 60577, t0 3/476/1215, 24h 3/90/1062. The t test was performed to determine statistical differences between the three tumor types. *$p < 0.05$, **$p < 0.01$, ***$p < 0.001$, ****$p < 0.0001$.

decrease in straightness for all three tumor types (Figure 4D). In HuHGS, HGS2, and 60577, the proportions for all behaviors were maintained at 24h compared to t0 (Figures 4D and S2D). At 24h, the migrating myeloid cell sub-population showed a significant increase in trajectory length in HGS2 and in speed in 60577 (Figure S3B), suggesting the mouse migrating myeloid cells are more motile after 24h.

Overall, these results show that $CD8^+$ T and myeloid cells are still motile after 24h *ex vivo*, despite movement changes. We conclude that we can use HuHGS, HGS2, and 60577 tumor slices in *ex vivo* behavior assays within 24h providing experiments include control conditions.

Lipopolysaccharide increases the motile behavior of $CD8^+$ T and myeloid cells in mouse and human *ex vivo* high-grade serous ovarian cancer tumors slices

We next assessed the ability of an *ex vivo* treatment to alter the dynamic behavior of $CD8^+$ T and myeloid cells. We chose LPS for its ability to alter macrophage polarization which in turn can regulate T cells. Tumor slices from HGSOC patients and HGS2 and 60577 mice were put in culture *ex vivo* immediately after slicing, treated or not with LPS for 24h and the movements of $CD8^+$ T and myeloid cells was monitored (Figures 5A, 5B, S4A, and S4B).

In HuHGS, HGS2, and 60577, LPS significantly increased trajectory length (+14.6%, +22.9%, and +42.7%, respectively) and speed (+14.7%, +35.9%, and +79.8%). In addition, LPS increased $CD8^+$ T cells trajectory straightness in the mouse models but decreased it in HuHGS (Figure 5C). To further investigate which populations of $CD8^+$ T cells are affected by LPS, we assessed the proportions of the different behavior and quantified their movements (Figures 5C, S4C, and S5A). LPS did not significantly alter the proportions of any behavior in any tumor type, suggesting the absence of a shift between static, wobbling, migrating, and long migrating behavior (Figures 5C and S4C). In HuHGS, consistent with the global increase in movements and the absence of change in the proportions of each behavior, both wobbling and migrating populations displayed increased movements (Figure S5A). In HGS2, the migrating and wobbling $CD8^+$ T cells displayed little change with LPS, however (Figure S5A).

In HGS2 and 60577, myeloid cells displayed significantly increased trajectory length (+25.7% and +35.8%, respectively), speed (+50.1% and +44.7%, respectively) and straightness upon LPS treatment (Figure 5D). In HuHGS, speed increased only by 5.6%, trajectory length was not affected and straightness decreased (Figure 5D), suggesting LPS had less impact on human $CD11b^+$ than on mouse $F4/80^+$ cells. Furthermore, LPS did not change the proportions of migrating, wobbling, long migrating, and static myeloid cells (Figures 5D and S5A). In addition, we observed no change in migrating myeloid cell trajectory length or speed in all three tumor types, suggesting changes in the overall population are driven by a stimulation of the wobbling population (Figure S5B).

These results show that LPS alters the movements of $CD8^+$ T and myeloid cells *ex vivo*. It also demonstrates that migrating and wobbling sub-groups of both cell types can respond differently to treatments.

Chemotherapy alters the motile behavior of $CD8^+$ T and myeloid cells in mouse and human high-grade serous ovarian cancer tumor slices

We have previously shown that chemotherapy alters myeloid and T cells activities and numbers in HGSOC.[12–14] Therefore, we also wished to analyze the impact of chemotherapy on the behavior of $CD8^+$ T and myeloid cells in HuHGS, HGS2, and 60577. We collected seventeen HuHGS omental tumors from five primary and twelve interval debulking surgeries (respectively pre- and post-chemotherapy). In addition, we treated HGS2 or 60577 mice *in vivo* with carboplatin plus paclitaxel and grouped omental tumors collected at different time points after treatment (Figure S6A). We compared the movements of $CD8^+$ T and myeloid cells in HuHGS pre- and post-chemotherapy (Figure 6A) and in HGS2 and 60577 mice from control and treated groups (Figure S6B).

In terms of $CD8^+$ cells, we observed a significant decrease in speed (−33.7%) and straightness in HuHGS in post compared to pre-chemotherapy tumors (Figure 6C). HGS2 and 60577 also displayed significantly decreased trajectory length (−14.7% and −38.4%), speed (−46.5% and −49.7%), and straightness for $CD8^+$ T cells in treated tumors compared to controls (Figure 6E). Analysis of the behavior proportions showed a significant increase in the proportion of wobbling $CD8^+$ T cells in post-chemotherapy HuHGS tumors compared to pre-chemotherapy HuHGS tumors (Figures 6C and S6D). The migrating human $CD8^+$

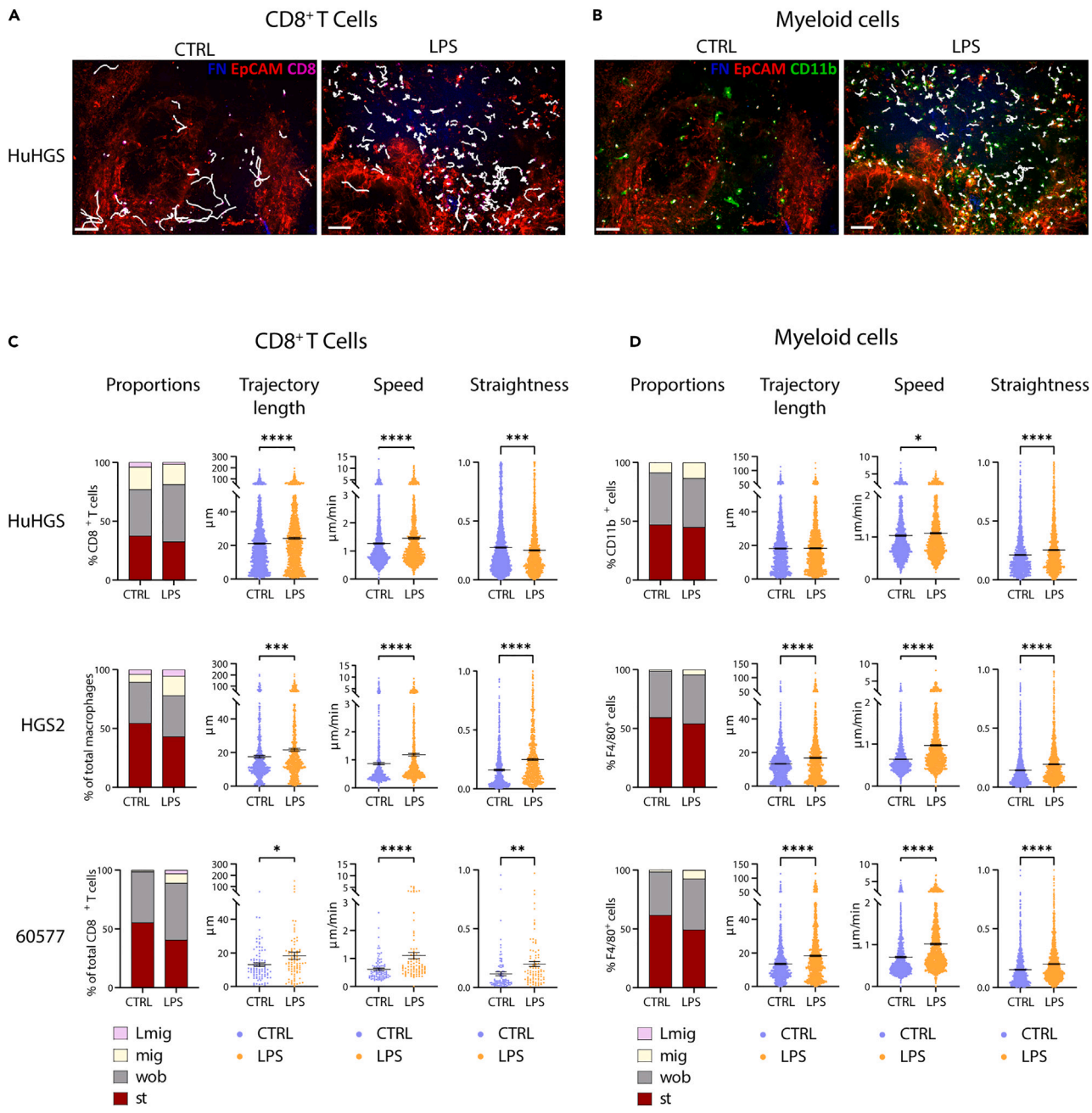

Figure 5. Impact of LPS on CD8$^+$ T and myeloid cell behavior in human and mouse *ex vivo* tumor slices

(A and B) Live human HGSOC tumor slices treated or not (CTRL) with LPS *ex vivo* for 24h stained for: fibronectin (blue), myeloid cells (green, CD11b); malignant cells (red, EpCAM); CD8$^+$ T cells (pink) and imaged in real-time. Tracks of CD8$^+$ T cells, (A), and myeloid cells, (B), are shown in white. Scale bars 50 µm.

(C and D) Proportions of the different types of behavior (red, st, static; gray, wob, wobbling; yellow, mig, migrating; pink, Lmig, long migrating), trajectory length, mean speed, and trajectory straightness in control (purple) and LPS-treated (orange) human HGSOC, HGS2, and 60577 tumor slices for (C), CD8$^+$ T cells and (D), myeloid cells (human, CD11b$^+$ cells; HGS2 and 60577, F4/80$^+$ cells). Histograms display the mean ± SEM. Number of tumors/CD8$^+$ T cells/myeloid cells for each model and condition: human, CTRL 10/2410/1558, LPS 6/1484/1785; HGS2, CTRL 8/731/1616, LPS 8/770/1746; 60577, CTRL 3/90/1062, LPS $^3/_8$9/1615. The t-test was performed to determine statistical differences between the three tumor types. *p < 0.05, **p < 0.01, ***p < 0.001, ****p < 0.0001.

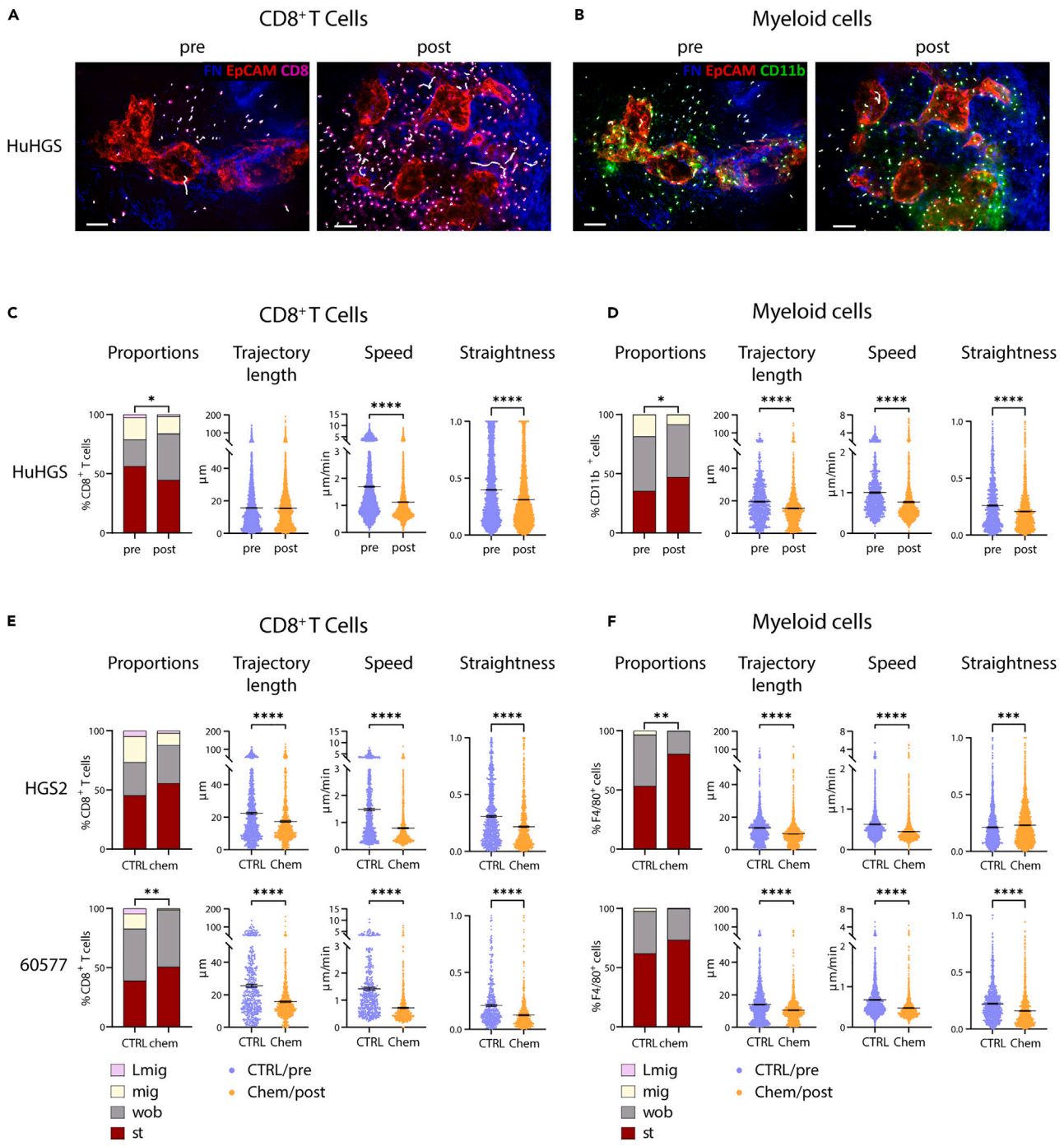

Figure 6. Impact of chemotherapy on CD8$^+$ T and myeloid cell behavior in human and mouse *ex vivo* tumor slices

(A and B) Live human HGSOC tumor slices from patients prior to (pre) or post-chemotherapy treatment (post) were stained for: fibronectin (blue), myeloid cells (green, CD11b); malignant cells (red, EpCAM); CD8$^+$ T cells (pink) and imaged in real-time. Tracks of CD8$^+$ T cells, (A), and myeloid cells, (B), are shown in white. Scale bars 50 µm.

(C–F) Proportions of the different types of behavior (red, st, static; gray, wob, wobbling; yellow, mig, migrating; pink, Lmig, long migrating), trajectory length, mean speed, and trajectory straightness in (C) – (D), pre (purple) and post (orange) chemotherapy human HGSOC tumor slices; (E) – (F), HGS2 and 60577 tumor slices from control mice (purple) or mice treated with carboplatin and paclitaxel *in vivo* (orange) for (C) and (E), CD8$^+$ T cells and (D) and (F), myeloid cells (human, CD11b$^+$ cells; HGS2 and 60577, F4/80$^+$ cells). Histograms display the mean ± SEM. Number of tumors/CD8$^+$ T cells/myeloid cells for each model and condition: human, pre 5/4594/1320, post 12/7474/1656; HGS2, CTRL 4/858/1466, Chem 7/907/2913; 60577, CTRL 5/476/1215, Chem 9/648/1075. The t-test was performed to determine statistical differences between the three tumor types. *p < 0.05, **p < 0.01, ***p < 0.001, ****p < 0.0001.

T cells displayed increased trajectory length and speed, while the wobbling population showed reduction in those metrics (Figure S7A). This suggests the wobbling population is responsible for the global decrease in $CD8^+$ T cell speed and that migrating and wobbling populations respond differently to chemotherapy. In 60577, a chemotherapy sensitive model[9] there was a significant decrease in the number of migrating and long migrating $CD8^+$ T cells. On the other hand, $CD8^+$ T cells from HGS2 tumors, a chemo-resistant model, did not show any difference in behavior proportions (Figures 6E and S6D).

Measurement of myeloid cell population movements showed a decrease of trajectory length (HuHGS −21.6%, HGS2 -28.1%, and 60577–24.8%) and speed (HuHGS −23.2%, HGS2 -29.0%, and 60577–29.8%) in all three tumor types (Figures 6D and 6F). There were less migrating myeloid cells in HuHGS post compared to pre-chemotherapy tumors (Figures 6B, 6D, and S6E). In addition, the chemo-resistant mouse model HGS2 displayed a decrease in all myeloid cell movements, while the chemo-sensitive model 60577 displayed no difference between control and treated groups (Figure 6F, S6C, and S6E). While the wobbling sub-population displayed decreased movements in all tumor types, the migrating cells displayed an increased speed in HuHGS and 60577 along with an increased trajectory length in HuHGS (Figure S7B). This suggested chemotherapy decreases the number of migrating myeloid cells in some tumor types but stimulated their motility.

To assess whether changes in $CD8^+$ T and myeloid cell behavior were due to killing of immune cells by the chemotherapy, we fixed sections from the HuHGS, HGS2, and 60577 tumors that were analyzed for cell migration and performed IHC for cleaved caspase-3, ccas3. There was no significant difference between pre- and post-chemotherapy levels of ccas3 in human tumors or between control and chemotherapy treated HGS2 tumors (Figure S6F). However there was an increase in apoptosis in 60577 tumors (Figure S6F) that are sensitive to chemotherapy.[9] To further study the effects of chemotherapy on the immune cell populations, we conducted flow cytometry on another cohort of human HGSOC biopsies and found no difference in the viability of $CD8^+$ T cells and $CD14^+HLADR^+$ macrophages comparing pre- and post-chemotherapy samples (Figure S6G). We conclude that post-chemotherapy $CD8^+$ T and myeloid cell behavior changes are unlikely to be due to changes in immune cell viability.

Overall, these results showed chemotherapy affects differently the migrating and wobbling cell populations and causes changes in the behavior of $CD8^+$ T and myeloid cells that vary in models with different chemotherapy sensitivity.

DISCUSSION

The high rate of recurrence in HGSOC patients[23] shows the necessity to better understand the TME in this disease and to design strategies to prevent relapse. To tackle this, efforts have been made in developing relevant HGSOC human pre-clinical models.[10,11,24] There is however growing need to develop models that encompass the whole of the human TME and enable the study of its dynamics.

Here, we addressed this need by further developing the tumor slice technique and present an experimental model for both mouse and human HGSOC that allows the assessment of the movements of cells contained within their native TME *ex vivo* for 24h. We report minimal loss of viability and reasonable immune cell stability. Those results are supported by previous studies on ovarian and other types of tumor slices, showing that in optimized culture conditions a small reduction in viability and in T cell content *ex vivo* are observed.[18,25,26] In addition, we report for the first time immune cell movement recorded and analyzed after 24h *ex vivo*. We show that despite $CD8^+$ T and myeloid cells displaying decreased motility, no significant change in behavior proportions was observed. We conclude this *ex vivo* model allows the study of cell behavior during 24h.

Migration of cytotoxic lymphocytes is an important function involved in the control of tumor growth, prognosis, and immunotherapy response[27–29] and has so far been the focus of $CD8^+$ T cell movement studies. However, we suggest that the approach to analyze these movements needs to be refined. We made the observation that some cells did not display migration but simply dynamic shape changes or non-directional migration, resulting in a wobbling motion. Here, we propose a semi-supervised method for separating the migrating from the non-migrating cells and refine this analysis by distinguishing four behavior categories: static, wobbling, migrating, and long migrating. We show wobbling and migrating cells often respond differently to treatments, suggesting they belong to distinct sub-populations. While each sub-group can be altered independently of the other, it is also possible to observe changes in behavior proportions,

suggesting these sub-groups are dynamic and that cells can alternate between different states. Moreover, an unsupervised analysis has previously revealed that morpho-dynamic traits are associated with specific sub-populations of leukocytes, harboring different cellular states or identities.[30] Likewise, in human organoids different behavioral T cell patterns have been reported reflecting phenotypic heterogeneity.[31] We therefore hypothesize that wobbling and migrating cells of one given cell type are two distinct populations harboring different cellular states and responses to treatments. Whether such differences are caused by changes in external determinants (e.g., ECM), changes in cell-cell interactions that physically impede cell movements, or differences in activation state or chemokine gradients[22,32,33] remains to be determined. For both $CD8^+$ T and myeloid cells, the wobbling state could result from the inability to migrate in a directional manner. In addition, wobbling myeloid cells could be probing the surrounding environment or interacting with malignant cells as previously reported for dendritic cells in murine lymph nodes.[34] For $CD8^+$ T cells, the wobbling state could also be due to migration-impeding interactions with B, antigen-presenting[35] or malignant cells when performing their killing function.[36,37]

The migration pattern of T cells reported here was similar to what has previously been shown in solid tumor, although with lower speed.[20,36,38] This shows restricted cytotoxic T cell migration in HGSOC and suggests improving their motility would benefit patients.

To our knowledge, this is the first time measurements of myeloid cell migration *ex vivo* have been reported, and our results showed lower speed than previously reported *in vivo*, in zebrafish and CT26 mouse tumors.[34,39–41] We noted that $CD11b^+$ cells in HuHGS were more migratory than $F4/80^+$ cells in mouse tumor slices. CD11b is expressed by all myeloid cells, including neutrophils, known to be more motile,[41] which could account for this difference.

Using our semi-supervised approach, we demonstrated the possibility of measuring changes in cell behavior after *ex vivo* treatment. LPS increased the movements of myeloid cells that is consistent with published *in vivo* data[42] and suggests M1-polarized have a distinct behavior from M2-polarized macrophages. We also report an impact on $CD8^+$ T cells, suggesting LPS stimulation of inflammation pathways affects cytotoxic T cell behavior, probably through activation of dendritic cells[43] or release of chemokines. LPS had similar effects in both human and mouse models, showing the relevance of the mouse models to study the impact of compounds on immune cell movements *ex vivo*.

Finally, we report an impact of chemotherapy on the behavior of $CD8^+$ T and myeloid cells. We show *in vivo* chemotherapy decreased the movements of both $CD8^+$ T and myeloid cells in all tumor types. Chemotherapy also increased the proportions of wobbling cells in the human biopsies. Although this could be due to impaired migration, it is also possible it is caused by increased cytotoxic activity of the T cells on the malignant cells. Furthermore, $CD8^+$ T cells were more affected by chemotherapy in the chemo-sensitive model 60577, while myeloid cells were more impacted in the chemo-resistant model HGS2. Increased wobbling $CD8^+$ T cells in HuHGS could be explained by an increase in cell-cell interactions, possibly in killing. We have previously shown chemotherapy decreases M2-polarized macrophage numbers[14] and activates $CD4^+$ T cells,[12] which suggests an activation of $CD8^+$ T cells. Further investigation is required to assess if the reduction in movements we report here are linked to changes in macrophage phenotype and $CD8^+$ T cell killing. The lack of difference in overall apoptosis and immune cell viability between pre- and post-chemotherapy suggests it is unlikely that the chemotherapy-induced changes in motility observed in human tumor slices are caused by a decrease in immune cell viability. We conclude chemotherapy may trigger changes of cell state, altering $CD8^+$ T and myeloid cell movements and that these cells may be differently affected in responsive and non-responsive tumors. Understanding the mechanisms behind such a differential effect could lead to strategies enhancing the anti-tumor phenotype of myeloid cells, T cell cytotoxic activity and the effect of chemotherapy.

With this study, we expand the tumor slice technique by analyzing the behavior of $CD8^+$ T and myeloid cells in HGSOC tumor slices after 24h *ex vivo*. We show this system can be used to assess the effect of treatments on immune cell movements and provide an in-depth approach to analyze cell behavior. Being able to integrate multiple outputs, including a treatment's effect on the dynamic aspect of the TME gives invaluable insight into the mechanism of drugs and their therapeutic potential in individual tumors. In addition, being able to reproduce, in the human tumor slices *ex vivo*, effects observed *in vivo* in the mouse, provides a stepping stone to translate mouse work to clinical trials.

Limitations of the study

The semi-supervised analysis presented here uses empirically determined thresholds. A fully unsupervised analysis would help further support our conclusions that $CD8^+$ T and myeloid cells can be categorized with four types of behavior: static, wobbling, migrating, and long migrating.

STAR★METHODS

Detailed methods are provided in the online version of this paper and include the following:

- KEY RESOURCES TABLE
- RESOURCE AVAILABILITY
  - Lead contact
  - Materials availability
  - Data and code availability
- EXPERIMENTAL MODEL AND SUBJECT DETAILS
  - Patient sample collection
  - Mouse experiments
  - Cell culture
- METHOD DETAILS
  - Slicing and *ex vivo* culture
  - Slice immunostaining and real-time imaging
  - Behaviour analysis
  - Behaviour categories
  - Behaviour data processing
  - Immunohistochemistry
  - Flow cytometry
- QUANTIFICATION AND STATISTICAL ANALYSIS

SUPPLEMENTAL INFORMATION

Supplemental information can be found online at https://doi.org/10.1016/j.isci.2023.106514.

ACKNOWLEDGMENTS

The authors would like to thank the surgeons of Barts Trust Oncology for their help in supplying human tumors. We wish to acknowledge Nadia Rahman and the BCI pathology core, Dr. Linda Hammond and the BCI microscopy core and the Biological Services Unit. We thank Dr. Chiara Berlato and Dr. Ganga Gopinathan for their technical help and Dr. Eleni Maniati for her help with R. We would also like to acknowledge Pr. Victoria Sanz-Moreno for sharing her expertise with cell movement. Finally, we are extremely grateful to the patients who donated samples and made this study possible. This work was funded by Cancer Research UK program grants (A16354, A25714, to F.R.B), by an Ovarian Cancer Research Alliance grant (648516 to B.M. and F.R.B), by Wellbeing of Women grants (ELS906 and RTF1103 to S.E), a Barts Charity grant (ECMG1B6R to R.M) and a Ligue Nationale Contre le Cancer grant (EL2020.LNCC to E.D).

AUTHOR CONTRIBUTIONS

F.B., E.D., F.L., and P.K. designed the project; F.L. designed and performed human and mouse tissue slice experiments; F.L and P.K. designed and performed mouse experiments; F.L designed and performed the cell movement analysis method; F.L., B.M., S.E., and R.M. provided human tumor supply; E.D., P.K., B.M., S.E., and R.M. made intellectual contributions; F.B and F.L. wrote the manuscript and all authors contributed to improving the manuscripts.

DECLARATION OF INTERESTS

F.L., P.K, B.M., S.E., and E.D. declare no competing interests. R.M. declares research funding from Barts Charity. R.M. declares research funding from Rosetrees Trust, Eve Appeal, GSK, Yorkshire Cancer Research outside this work, honorarium for advisory board membership from Astrazeneca/Merck Sharp & Dohme/Everything Genetics limited. F.B. declares being on the Scientific Advisory Board of iOmx Therapeutics AG.

INCLUSION AND DIVERSITY

We support inclusive, diverse, and equitable conduct of research.

Received: November 7, 2022
Revised: March 3, 2023
Accepted: March 27, 2023
Published: March 29, 2023

REFERENCES

1. Boyle, S.T., Johan, M.Z., and Samuel, M.S. (2020). Tumour-directed microenvironment remodelling at a glance. J. Cell Sci. *133*, jcs247783. https://doi.org/10.1242/jcs.247783.

2. Roma-Rodrigues, C., Mendes, R., Baptista, P.V., and Fernandes, A.R. (2019). Targeting tumor microenvironment for cancer therapy. Int. J. Mol. Sci. *20*, 840. https://doi.org/10.3390/ijms20040840.

3. Li, J., Eu, J.Q., Kong, L.R., Wang, L., Lim, Y.C., Goh, B.C., and Wong, A.L.A. (2020). Targeting metabolism in cancer cells and the tumour microenvironment for cancer therapy. Molecules *25*, 4831. https://doi.org/10.3390/molecules25204831.

4. Lheureux, S., Gourley, C., Vergote, I., and Oza, A.M. (2019). Epithelial ovarian cancer. Lancet *393*, 1240–1253. https://doi.org/10.1016/s0140-6736(18)32552-2.

5. Bowtell, D.D., Böhm, S., Ahmed, A.A., Aspuria, P.-J., Bast, R.C., Beral, V., Berek, J.S., Birrer, M.J., Blagden, S., Bookman, M.A., et al. (2015). Rethinking ovarian cancer II: reducing mortality from high-grade serous ovarian cancer. Nat. Rev. Cancer *15*, 668–679. https://doi.org/10.1038/nrc4019.

6. Gockley, A., Melamed, A., Bregar, A.J., Clemmer, J.T., Birrer, M., Schorge, J.O., Del Carmen, M.G., and Rauh-Hain, J.A. (2017). Outcomes of women with high-grade and low-grade advanced-stage serous epithelial ovarian cancer. Obstet. Gynecol. *129*, 439–447. https://doi.org/10.1097/aog.0000000000001867.

7. Pearce, O.M.T., Delaine-Smith, R.M., Maniati, E., Nichols, S., Wang, J., Böhm, S., Rajeeve, V., Ullah, D., Chakravarty, P., Jones, R.R., et al. (2018). Deconstruction of a metastatic tumor microenvironment reveals a common matrix response in human cancers. Cancer Discov. *8*, 304–319. https://doi.org/10.1158/2159-8290.cd-17-0284.

8. Olbrecht, S., Busschaert, P., Qian, J., Vanderstichele, A., Loverix, L., Van Gorp, T., Van Nieuwenhuysen, E., Han, S., Van Den Broeck, A., Coosemans, A., et al. (2021). High-grade serous tubo-ovarian cancer refined with single-cell RNA sequencing: specific cell subtypes influence survival and determine molecular subtype classification. Genome Med. *13*, 111. https://doi.org/10.1186/s13073-021-00922-x.

9. Maniati, E., Berlato, C., Gopinathan, G., Heath, O., Kotantaki, P., Lakhani, A., McDermott, J., Pegrum, C., Delaine-Smith, R.M., Pearce, O.M.T., et al. (2020). Mouse ovarian cancer models recapitulate the human tumor microenvironment and patient response to treatment. Cell Rep. *30*, 525–540.e7. https://doi.org/10.1016/j.celrep.2019.12.034.

10. Malacrida, B., Nichols, S., Maniati, E., Jones, R., Delanie-Smith, R., Roozitalab, R., Tyler, E.J., Thomas, M., Boot, G., Mackerodt, J., et al. (2021). A human multi-cellular model shows how platelets drive production of diseased extracellular matrix and tissue invasion. iScience *24*, 102676. https://doi.org/10.1016/j.isci.2021.102676.

11. Delaine-Smith, R.M., Maniati, E., Malacrida, B., Nichols, S., Roozitalab, R., Jones, R.R., Lecker, L.S.M., Pearce, O.M.T., Knight, M.M., and Balkwill, F.R. (2021). Modelling TGFβR and Hh pathway regulation of prognostic matrisome molecules in ovarian cancer. iScience *24*, 102674. https://doi.org/10.1016/j.isci.2021.102674.

12. Böhm, S., Montfort, A., Pearce, O.M.T., Topping, J., Chakravarty, P., Everitt, G.L.A., Clear, A., McDermott, J.R., Ennis, D., Dowe, T., et al. (2016). Neoadjuvant chemotherapy modulates the immune microenvironment in metastases of tubo-ovarian high-grade serous carcinoma. Clin. Cancer Res. *22*, 3025–3036. https://doi.org/10.1158/1078-0432.CCR-15-2657.

13. Montfort, A., Pearce, O., Maniati, E., Vincent, B.G., Bixby, L., Böhm, S., Dowe, T., Wilkes, E.H., Chakravarty, P., et al. (2017). A strong B-cell response is part of the immune landscape in human high-grade serous ovarian metastases. Clin. Cancer Res. *23*, 250–262. https://doi.org/10.1158/1078-0432.CCR-16-0081.

14. Heath, O., Berlato, C., Maniati, E., Lakhani, A., Pegrum, C., Kotantaki, P., Elorbany, S., Böhm, S., Barry, S.T., Annibaldi, A., et al. (2021). Chemotherapy induces tumor-associated macrophages that aid adaptive immune responses in ovarian cancer. Cancer Immunol. Res. *9*, 665–681. https://doi.org/10.1158/2326-6066.cir-20-0968.

15. Gopinathan, G., Milagre, C., Pearce, O.M.T., Reynolds, L.E., Hodivala-Dilke, K., Leinster, D.A., Zhong, H., Hollingsworth, R.E., Thompson, R., Whiteford, J.R., and Balkwill, F. (2015). Interleukin-6 stimulates defective angiogenesis. Cancer Res. *75*, 3098–3107. https://doi.org/10.1158/0008-5472.can-15-1227.

16. Gopinathan, G., Berlato, C., Lakhani, A., Szabova, L., Pegrum, C., Pedrosa, A.R., Laforets, F., Maniati, E., and Balkwill, F.R. (2022). Immune mechanisms of resistance to cediranib in ovarian cancer. Mol. Cancer Ther. *21*, 1030–1043. https://doi.org/10.1158/1535-7163.Mct-21-0689.

17. Meijer, A., Kruyt, F.A.E., Van Der Zee, A.G.J., Hollema, H., Le, P., Ten Hoor, K.A., Groothuis, G.M.M., Quax, W.J., De Vries, E.G.E., and De Jong, S. (2013). Nutlin-3 preferentially sensitises wild-type p53-expressing cancer cells to DR5-selective TRAIL over rhTRAIL. Br. J. Cancer *109*, 2685–2695. https://doi.org/10.1038/bjc.2013.636.

18. Lheureux, S., N'Diaye, M., Blanc-Fournier, C., Dugué, A.E., Clarisse, B., Dutoit, S., Giffard, F., Abeilard, E., Briand, M., Labiche, A., et al. (2015). Identification of predictive factors of response to the BH3-mimetic molecule ABT-737: anex vivoexperiment in human serous ovarian carcinoma. Int. J. Cancer *136*, E340–E350. https://doi.org/10.1002/ijc.29104.

19. Peranzoni, E., Bougherara, H., Barrin, S., Mansuet-Lupo, A., Alifano, M., Damotte, D., and Donnadieu, E. (2017). Ex vivo imaging of resident CD8 T lymphocytes in human lung tumor slices using confocal microscopy. J. Vis. Exp. e55709. https://doi.org/10.3791/55709.

20. Bougherara, H., Mansuet-Lupo, A., Alifano, M., Ngô, C., Damotte, D., Le Frère-Belda, M.A., Donnadieu, E., and Peranzoni, E. (2015). Real-time imaging of resident T cells in human lung and ovarian carcinomas reveals how different tumor microenvironments control T lymphocyte migration. Front. Immunol. *6*, 500. https://doi.org/10.3389/fimmu.2015.00500.

21. Salmon, H., Franciszkiewicz, K., Damotte, D., Dieu-Nosjean, M.-C., Validire, P., Trautmann, A., Mami-Chouaib, F., and Donnadieu, E. (2012). Matrix architecture defines the preferential localization and migration of T cells into the stroma of human lung tumors. J. Clin. Invest. *122*, 899–910. https://doi.org/10.1172/JCI45817.

22. Salmon, H., and Donnadieu, E. (2012). Within tumors, interactions between T cells and tumor cells are impeded by the extracellular matrix. OncoImmunology *1*, 992–994. https://doi.org/10.4161/onci.20239.

23. Ledermann, J.A., Raja, F.A., Fotopoulou, C., Gonzalez-Martin, A., Colombo, N., and Sessa, C.; ESMO Guidelines Working Group (2013). Newly diagnosed and relapsed epithelial ovarian carcinoma: ESMO Clinical Practice Guidelines for diagnosis, treatment and follow-up. Ann. Oncol. *24*, vi24–vi32. https://doi.org/10.1093/annonc/mdt333.

24. Maenhoudt, N., Defraye, C., Boretto, M., Jan, Z., Heremans, R., Boeckx, B., Hermans, F., Arijs, I., Cox, B., Van Nieuwenhuysen, E., et al. (2020). Developing organoids from ovarian cancer as experimental and preclinical models. Stem Cell Rep. *14*, 717–729. https://doi.org/10.1016/j.stemcr.2020.03.004.

25. Estes, J.M., Oliver, P.G., Straughn, J.M., Zhou, T., Wang, W., Grizzle, W.E., Alvarez, R.D., Stockard, C.R., LoBuglio, A.F., and Buchsbaum, D.J. (2007). Efficacy of anti-death receptor 5 (DR5) antibody (TRA-8) against primary human ovarian carcinoma using a novel ex vivo tissue slice model. Gynecol. Oncol. *105*, 291–298. https://doi.org/10.1016/j.ygyno.2006.12.033.

26. Sivakumar, R., Chan, M., Shin, J.S., Nishida-Aoki, N., Kenerson, H.L., Elemento, O., Beltran, H., Yeung, R., and Gujral, T.S. (2019). Organotypic tumor slice cultures provide a versatile platform for immuno-oncology and drug discovery. OncoImmunology *8*, e1670019. https://doi.org/10.1080/2162402x.2019.1670019.

27. Peranzoni, E., Lemoine, J., Vimeux, L., Feuillet, V., Barrin, S., Kantari-Mimoun, C., Bercovici, N., Guérin, M., Biton, J., Ouakrim, H., et al. (2018). Macrophages impede CD8 T cells from reaching tumor cells and limit the efficacy of anti–PD-1 treatment. Proc. Natl. Acad. Sci. USA *115*, E4041–E4050. https://doi.org/10.1073/pnas.1720948115.

28. Gooden, M.J.M., De Bock, G.H., Leffers, N., Daemen, T., and Nijman, H.W. (2011). The prognostic influence of tumour-infiltrating lymphocytes in cancer: a systematic review with meta-analysis. Br. J. Cancer *105*, 93–103. https://doi.org/10.1038/bjc.2011.189.

29. Golstein, P., and Griffiths, G.M. (2018). An early history of T cell-mediated cytotoxicity. Nat. Rev. Immunol. *18*, 527–535. https://doi.org/10.1038/s41577-018-0009-3.

30. Crainiciuc, G., Palomino-Segura, M., Molina-Moreno, M., Sicilia, J., Aragones, D.G., Li, J.L.Y., Madurga, R., Adrover, J.M., Aroca-Crevillén, A., Martin-Salamanca, S., et al. (2022). Behavioural immune landscapes of inflammation. Nature *601*, 415–421. https://doi.org/10.1038/s41586-021-04263-y.

31. Dekkers, J.F., Alieva, M., Cleven, A., Keramati, F., Wezenaar, A.K.L., Van Vliet, E.J., Puschhof, J., Brazda, P., Johanna, I., Meringa, A.D., et al. (2023). Uncovering the mode of action of engineered T cells in patient cancer organoids. Nat. Biotechnol. *41*, 60–69. https://doi.org/10.1038/s41587-022-01397-w.

32. Donnadieu, E., Dupré, L., Pinho, L.G., and Cotta-De-Almeida, V. (2020). Surmounting the obstacles that impede effective CAR T cell trafficking to solid tumors. J. Leukoc. Biol. *108*, 1067–1079. https://doi.org/10.1002/jlb.1mr0520-746r.

33. Nicolas-Boluda, A., Vaquero, J., Vimeux, L., Guilbert, T., Barrin, S., Kantari-Mimoun, C., Ponzo, M., Renault, G., Deptula, P., Pogoda, K., et al. (2021). Tumor stiffening reversion through collagen crosslinking inhibition improves T cell migration and anti-PD-1 treatment. Elife *10*, e58688. https://doi.org/10.7554/elife.58688.

34. Leimgruber, A., Berger, C., Cortez-Retamozo, V., Etzrodt, M., Newton, A.P., Waterman, P., Figueiredo, J.L., Kohler, R.H., Elpek, N., Mempel, T.R., et al. (2009). Behavior of endogenous tumor-associated macrophages assessed in vivo using a functionalized nanoparticle. Neoplasia *11*, 459–468. https://doi.org/10.1593/neo.459.

35. Mempel, T.R., Pittet, M.J., Khazaie, K., Weninger, W., Weissleder, R., Von Boehmer, H., and Von Andrian, U.H. (2006). Regulatory T cells reversibly suppress cytotoxic T cell function independent of effector differentiation. Immunity *25*, 129–141. https://doi.org/10.1016/j.immuni.2006.04.015.

36. Mrass, P., Takano, H., Ng, L.G., Daxini, S., Lasaro, M.O., Iparraguirre, A., Cavanagh, L.L., Von Andrian, U.H., Ertl, H.C.J., Haydon, P.G., and Weninger, W. (2006). Random migration precedes stable target cell interactions of tumor-infiltrating T cells. J. Exp. Med. *203*, 2749–2761. https://doi.org/10.1084/jem.20060710.

37. Breart, B., Lemaître, F., Celli, S., and Bousso, P. (2008). Two-photon imaging of intratumoral CD8+ T cell cytotoxic activity during adoptive T cell therapy in mice. J. Clin. Invest. *118*, 1390–1397. https://doi.org/10.1172/jci34388.

38. Boissonnas, A., Fetler, L., Zeelenberg, I.S., Hugues, S., and Amigorena, S. (2007). In vivo imaging of cytotoxic T cell infiltration and elimination of a solid tumor. J. Exp. Med. *204*, 345–356. https://doi.org/10.1084/jem.20061890.

39. Kaveh, A., Bruton, F.A., Buckley, C., Oremek, M.E.M., Tucker, C.S., Mullins, J.J., Taylor, J.M., Rossi, A.G., and Denvir, M.A. (2020). Live imaging of heart injury in larval zebrafish reveals a multi-stage model of neutrophil and macrophage migration. Front. Cell Dev. Biol. *8*, 579943. https://doi.org/10.3389/fcell.2020.579943.

40. Travnickova, J., Nhim, S., Abdellaoui, N., Djouad, F., Nguyen-Chi, M., Parmeggiani, A., and Kissa, K. (2021). Macrophage morphological plasticity and migration is Rac signalling and MMP9 dependant. Sci. Rep. *11*, 10123. https://doi.org/10.1038/s41598-021-88961-7.

41. Barros-Becker, F., Lam, P.-Y., Fisher, R., and Huttenlocher, A. (2017). Live imaging reveals distinct modes of neutrophil and macrophage migration within interstitial tissues. J. Cell Sci. *130*, 3801–3808. https://doi.org/10.1242/jcs.206128.

42. Shen, C., Chen, J.H., Lee, Y., Hassan, M.M., Kim, S.J., Choi, E.Y., Hong, S.-T., Park, B.-H., and Park, J.H. (2018). mTOR- and SGK-mediated connexin 43 expression participates in lipopolysaccharide-stimulated macrophage migration through the iNOS/src/FAK Axis. J. Immunol. *201*, 2986–2997. https://doi.org/10.4049/jimmunol.1700954.

43. Hassanzadeh-Kiabi, N., Yáñez, A., Dang, I., Martins, G.A., Underhill, D.M., and Goodridge, H.S. (2017). Autocrine type I IFN signaling in dendritic cells stimulated with fungal β-glucans or lipopolysaccharide promotes CD8 T cell activation. J. Immunol. *198*, 375–382. https://doi.org/10.4049/jimmunol.1601143.

44. Szabova, L., Bupp, S., Kamal, M., Householder, D.B., Hernandez, L., Schlomer, J.J., Baran, M.L., Yi, M., Stephens, R.M., Annunziata, C.M., et al. (2014). Pathway-specific engineered mouse allograft models functionally recapitulate human serous epithelial ovarian cancer. PLoS One *9*, e95649. https://doi.org/10.1371/journal.pone.0095649.

STAR★METHODS

KEY RESOURCES TABLE

REAGENT or RESOURCE	SOURCE	IDENTIFIER
Antibodies		
Human IL-6 Antibody	R&D systems	Cat# AF-206-NA; RRID:AB_354392
InVivoMAb anti-mouse IL-6 clone MP5-20F3	BioXCell	Cat# BE0046; RRID:AB_1107709
InVivoMAb rat IgG1 isotype control, anti-horseradish peroxidase (isotype control for anti-mouse IL-6)	BioXCell	Cat# BE0088; RRID:AB_1107775
Alexa Fluor® 647 anti-human CD8 Antibody	BioLegend	Cat# 344725; RRID:AB_2563451
CD8a Antibody, anti-mouse, APC, REAfinity™	Miltenyi Biotec®	Cat# 130-117-664; RRID:AB_2728016
CD326 (EpCAM) Monoclonal Antibody (MH99), Alexa Fluor™ 488, eBioscience™	ThermoFisher Scientific	Cat# 53-8326-42; RRID:AB_11219279
Recombinant Anti-Cytokeratin 8 antibody [EP1628Y] - Cytoskeleton Marker	abcam	Cat# ab53280; RRID:AB_869901
Recombinant Anti-Cytokeratin 14 antibody [EPR17350] - Cytoskeleton Marker	abcam	Cat# ab181595; RRID:AB_2811031
Alexa Fluor® 594 anti-human CD11b Antibody	BioLegend	Cat# 301340; RRID:AB_2563208
F4/80 antibody | Cl:A3-1	BioRad	Cat# MCA497G; RRID:AB_872005
Anti-Fibronectin antibody	abcam	Cat# ab23750; RRID:AB_447655
Fibronectin Antibody (HFN7.1) [Alexa Fluor® 405]	Novus biologicals	Cat# NBP2-34633AF405; RRID: N/A
AffiniPure Fab Fragment Goat Anti-Mouse IgG (H+L)	Stratech	Cat# 115-007-003; RRID:AB_2338476
CD3, Polyclonal, Unconjugated, Affinity isolated	Agilent	Cat# A045229-2; RRID:AB_2335677
Recombinant Anti-CD8 alpha antibody [EPR20305]	abcam	Cat# ab209775; RRID:AB_2860566
Recombinant Anti-CD4 antibody [EPR19514]	abcam	Cat# ab183685; RRID:AB_2686917
F4/80 antibody | Cl:A3-1 (AlexaFluor® 488)	BioRad	Cat# MCA497A488T; RRID:AB_1102554
CD68 Monoclonal Antibody (KP1)	ThermoFisher Scientific	Cat# 14-0688-82; RRID:AB_11151139
Anti-Ki67 antibody [SP6]	abcam	Cat# ab16667; RRID:AB_302459
Cleaved Caspase-3 (Asp175) (5A1E) Rabbit mAb	Cell Signaling Technology	Cat# 9664S; RRID:AB_2070042
CD206 Antibody | MR5D3	BioRad	Cat# MCA2235; RRID:AB_324622
CD206 Monoclonal Antibody (15-2)	ThermoFisher Scientific	Cat# MA1-35936; RRID:AB_2144918
PerCP anti-human CD45 Antibody	Biolegend	Cat# 304026; RRID: AB_893337
Alexa Fluor® 700 anti-human HLA-DR Antibody	Biolegend	Cat# 307626; RRID: AB_493771
Brilliant Violet 650™ anti-human HLA-DR Antibody	Biolegend	Cat# 307650; RRID: AB_2563828
APC anti-human CD4 Antibody	Biolegend	Cat# 357408; RRID: AB_2565660
APC/Fire™ 750 anti-human CD16 Antibody	Biolegend	Cat# 360726; RRID: AB_2632868
Brilliant Violet 650™ anti-human CD8 Antibody	Biolegend	Cat# 344730; RRID: AB_2564510
Brilliant Violet 711™ anti-human CD206 (MMR) Antibody	Biolegend	Cat# 321135; RRID: AB_2687199
Brilliant Violet 785™ anti-human CD14 Antibody	Biolegend	Cat# 301839; RRID: AB_2561366
PE anti-human CD163 Antibody	Biolegend	Cat# 333606; RRID: AB_1134002
PE Mouse Anti-Human CD123 Clone 7G3 (RUO)	BD Pharmingen™	Cat# 554529; RRID: AB_395457
PE/Cyanine5 anti-human CD3 Antibody	Biolegend	Cat# 300310; RRID: AB_314046
CD19 Monoclonal Antibody (SJ25C1), PE-Cyanine5.5, eBioscience™	Thermofisher	Cat# 35-0198-42; RRID: AB_11218903
PE anti-human CD274 (B7-H1, PD-L1) Antibody	Biolegend	Cat# 329706; RRID: AB_940368
FcR Blocking Reagent, human	Miltenyi Biotec®v	Cat# 130-059-901; RRID: AB_2892112
Human TruStain FcX™	BioLegend	Cat# 422302; RRID: AB_2818986

(*Continued on next page*)

Continued

REAGENT or RESOURCE	SOURCE	IDENTIFIER
Biological Samples		
Human high grade serous ovarian cancer omental metastasis samples		
Chemicals, Peptides, and Recombinant Proteins		
DMEM/F-12, GlutaMAX™	Gibco™	Cat# 31331093
Fetal Bovine Serum, qualified, heat inactivated, USDA-approved regions	Gibco™	Cat# 10438026
human serum	Merck	Cat# H4522
Penicillin-Streptomycin	Merck	Cat# 11074440001
Insulin-Transferrin-Selenium-Sodium Pyruvate (ITS-A) (100X)	Gibco™	Cat# 51300044
hydrocortisone	Merck	Cat# H0135
Epidermal Growth Factor from murine submaxillary gland	Merck	Cat# E4127
Human EGF, AOF Recombinant Protein	ThermoFisher Scientific	Cat# PHG6045
Antibiotic-Antimycotic	Gibco™	Cat# 15240062
O-Phosphorylethanolamine	Merck	Cat# P0503
3,3′,5-Triiodo-L-thyronine sodium salt	Merck	Cat# T6397
Fetuin from fetal bovine serum	Merck	Cat# F2379
Bovine Serum Albumin (low endotoxin)	Merck	Cat# A2058
LPS-EK (LPS from *E. coli* K12)	InvivoGen	Cat# tlrl-eklps
Normal Goat IgG Control (isotypic control for anti-human IL-6)	R&D systems	Cat# AB-108-C
RPMI 1640 Medium, no phenol red	ThermoFisher Scientific	Cat# 11835105
10% neutral buffered formalin	Merck	Cat# HT501128-4L
Agarose type VII-A, low gelling temperature	Merck	Cat# A0701
Invitrogen™ UltraPure™ Agarose	Fisher Scientific	Cat# 10264544
Proteinase K (Fungal)	ThermoFisher Scientific	Cat# 25530015
Antigen unmasking solution, citrate based	Vector Laboratories	Cat# H-3300
Antigen Retrieval Buffer (100X Tris-EDTA Buffer, pH 9.0)	abcam	Cat# ab93684
Methanol	Fisher Scientific	Cat# M/4000/PB17
Ethanol absolute	Fisher Scientific	Cat# E/0650DF/17
Xylene	Fisher Scientific	Cat# 10588070
Hydrogen Peroxide 30% (w/v) (100 Volumes), Extra Pure SLR, Fisher Chemical	Fisher Scientific	Cat# H/1750/15 (10687022)
Bovine Serum Albumin	Merck	Cat# A4503
Goat Serum, New Zealand origin	Gibco™	Cat# 16210064
Hematoxylin Solution, Gill No. 1	Merck	Cat# GHS1128-4L
Vector Methyl Green	Vector Laboratories	Cat# H-3402
DPX Mountant for histology	Merck	Cat# 6522
carboplatin	Hospira UK limited	Cat# 61703-0339
paclitaxel	Hospira UK limited	Cat# 61703-0342
Koliphor® EL	Merck	Cat# C5135
Sodium Chloride - Solution (0.9%), sterile	PanReac AppliChem	Cat# A1671
Triton™ X-100	Merck	Cat# T8787
0.5M EDTA pH 8.0 0.2µm filtered	ThermoFisher Scientific	Cat# AM9262
Trizma® base	Merck	Cat# T1503

(*Continued on next page*)

Continued

REAGENT or RESOURCE	SOURCE	IDENTIFIER
Critical Commercial Assays		
ImmPRESS® HRP Goat Anti-Rat IgG, Mouse adsorbed Polymer Detection Kit, Peroxidase	Vector Laboratories	Cat# MP-7444
ImmPRESS® HRP Goat Anti-Mouse IgG Polymer Detection Kit, Peroxidase	Vector Laboratories	Cat# MP-7452
ImmPRESS[R] HRP Goat Anti-Rabbit IgG Polymer Detection Kit, Peroxidase	Vector Laboratories	Cat# MP-7451
DyLight® 594 Fast Conjugation Kit	abcam	Cat# ab201801
DyLight® 405 Fast Conjugation Kit	abcam	Cat# ab201798
Tumor Dissociation Kit, human	Miltenyi biotec®	Cat# 130-095-929
gentleMACS™ Dissociator		Cat# 130-093-235
gentleMACS™ C- tubes	Miltenyi biotec®	Cat# 130-093-237
eBioscience™ 10X RBC Lysis Buffer (Multi-species)	ThermoFisher Scientific	Cat# 00-4300-54
eBioscience™ Fixable Viability Dye eFluor™ 506	eBioscience	Cat# v65-0866-18 RRID:
Experimental models: Cell lines		
HGS2	Laboratory of F. Balkwill	Maniati et al., 2020[9]
60577	Laboratory of F. Balkwill	Maniati et al., 2020[9]
Experimental models: mouse strains		
C57/Bl6J mice	Charles River	N/A
FBV mice	Charles River	N/A
Softwares and Algorithms		
Definiens® software	(Definiens AG, Germany)	http://www.astrazeneca.com
Panoramic Viewer 1.15.4	3DHISTECH, Hungary	https://pannoramic-viewer.software.informer.com/download/
NPD.view 2.7.25 software	Hammamatsu	https://www.hamamatsu.com/eu/en/product/type/U12388-01/index.html
R v4.0.4	N/A	http://www.R-project.org
R studio v1.4.1106	N/A	https://www.rstudio.com/products/rstudio/
tidyverse	N/A	https://www.tidyverse.org/
canceR	N/A	https://www.bioconductor.org/packages/release/bioc/html/canceR.html
Graphpad Prism, San Diego, CA version 9.0.0	N/A	https://www.graphpad.com
NIS-Elements	Nikon	https://www.microscope.healthcare.nikon.com/products/software/nis-elements
QuPath 0.2.3	N/A	https://qupath.github.io/
FlowJo Version 10.7.3	Treestar inc	https://www.flowjo.com/
Illustrator 2023	Adobe	https://www.adobe.com/uk/products/illustrator.html
Biorender.com	Biorender	https://www.biorender.com
Other		
35 mm Dish | No. 1.5 Coverslip | 20 mm Glass Diameter | Uncoated	MatTek	Cat# P35G-1.5-20-C
Peel-A-Way™ embedding molds	Merck	Cat# E6032
Millicell Cell Culture Insert, 30 mm, hydrophilic PTFE, 0.4 μm	Merck	Cat# PICM0RG50
M2.5 Stainless Steel Form A Washers	CPC UK	Cat# FN00783

(*Continued on next page*)

Continued

REAGENT or RESOURCE	SOURCE	IDENTIFIER
A2 Stainless Steel Washers (Form A) / M4	UK Stainless	none
Slice Anchor - Flat Stainless Steel for RC-41 Chamber, 1.5 mm, SHD-41/15	Warner Instruments	Cat# 641418
Slice Anchor - Flat Stainless Steel for RC-41 Chamber, 1.5 mm, SHD-41/10	Warner Instruments	Cat# 641419
Graefe Forceps	Fine Science Tools	Cat# 11050-10
Nikon Eclipse TE	Nikon	N/A
3DHISTECH Panoramic 250 digital slide scanner	3DHISTECH, Hungary	N/A
Hamamatsu NanoZoomer S210 Slide-Scanner	Hammamatsu	N/A
Peristaltic pump 120S/DM2	Watson and Marlow	Cat# 010.6131.M20
Vibratome VT1200S	Leica Biosystems	N/A
LSR fortessa cell analyser	(BD Bioscience	N/A

RESOURCE AVAILABILITY

Lead contact

Further information regarding resources and reagents should be addressed to the lead contact Frances Balkwill (f.balkwill@qmul.ac.uk).

Materials availability

No new reagent or material have been generated in this study.

Data and code availability

- All data reported in this paper will be shared by the lead contact upon request.
- Original annotated R scripts enabling cell movement analysis can be requested from the lead contact.
- Any additional information required to re-analyse the data reported in this paper is available from the lead contact upon request.

EXPERIMENTAL MODEL AND SUBJECT DETAILS

Patient sample collection

Fresh high grade serous ovarian cancer samples were kindly donated by patients undergoing primary, intermediary or delayed debulking surgery at St. George's University and Barts Health NHS Trust hospitals, after providing written informed consent. Experiments were performed under studies approved by a UK national review board (REC 10/H0304/14, 15/EE/0151 and 17/LO/0405). Tumour samples collected were judged to be surplus to diagnosis or therapeutic purposes by a pathologist or lead surgeon. Collection of samples observed the declaration of Helsinki and the international ethical guidelines for biomedical research involving human subject. Tumour samples were transported from the hospital to the laboratory on ice. Tumour displaying too high fat content or too fibrotic could not be sliced and were therefore excluded. We also excluded tumours displaying necrosis. This study therefore included 17 tumours: 5 pre (primary debulking surgery) and 12 post chemotherapy (intermediary or delayed debulking surgery).

Mouse experiments

Mouse experiments observed guideline provided by the ethics committees of Queen Mary University of London (QMUL) and under the Home Office project licence PBE3719B3. Friend leukemia virus (FVB) and C57BL/6J female mice were ordered from Charles River UK and were 9 weeks old at the start of the study. Animals were randomly assigned to treatment groups. Prior to injection, cells were trypsinised in 0.05% trypsin-EDTA, trypsin was neutralised in culture medium, and cells were counted and resuspended in PBS. 10^7 cells were intraperitoneally (i.p.) injected in FVB (60577) or C57BL/6J (HGS2) mice as previously described.[9,44] Mice underwent treatment by i.p. injection from week 3 (60577) or week 7 (HGS2) post cell injection, with carboplatin 20mg/kg and paclitaxel 10mg/kg or control vehicles (0.9% sodium chloride

and ethanol:Koliphor®EL 1:1) in 300µL once weekly for 3 weeks. Mice were sacrificed either 1, 7 or 21 days after the last dose of chemotherapy, or when they reached humane endpoint as described in the licence. Tumours were collected in ice cold RPMI1640 medium.

Cell culture

HGS2 and 60577 cells were grown in DMEM:F12 1:1 with glutamax, supplemented with 4% fetal bovine serum (FBS), 1X Pen-Strep, 1X antibiotic-antimycotic, 1X insulin/transferrin/selenium, 0.1µg/mL hydrocortisone, 20ng/mL murine EGF.

METHOD DETAILS

Slicing and *ex vivo* culture

The slicing method was adapted from Bougherara et al.[20] Tumours were cut in small pieces (around 3x3x8mm) and embedded in PBS with 5% low melting point agarose, submerged in ice cold PBS and sliced with a Vibratome (Leica, VT1200S), with blade speed set on 0.3mm/s, amplitude 1.5mm and thickness of slices 350µm. For some patient tumours, due to high fat content or high stiffness, blade speed was lowered to 0.2mm/s and amplitude to 1mm. Slices were either immediately fixed in formalin 10% or plated on 0.4 µm organotypic inserts in RPMI 1640 supplemented with 5% FBS or 5% human serum, 1X Pen-Strep, 1X antibiotic-antimycotic, 2X insulin/transferrin/selenium, 0.1µg/mL hydrocortisone, 20ng/mL murine EGF or human EGF, ethanolamine 10µM, O-phosphorylethanolamine 10µM, 1X minimal essential medium (MEM) vitamins, 3,3',5-triiodo-Lthyronine 100pM, fetuin 12.5µg/mL, BSA 2mg/mL and placed in culture at 37°C with 5% CO2. 1-5 slices were placed in each well of a 6-wells plate and medium was changed daily. Slices were treated or not with LPS 100ng/mL or for 24h and subsequently fixed in formalin 10% or immunostained.

Slice immunostaining and real-time imaging

For imaging at t0, slices were left at least 10 min in culture prior to immunostaining. Slices were transferred to a coated plastic petri dish and a stainless steel ring washer was placed around the tumour slice to hold drops of blocking reagent, antibody mix and washing medium. FcR receptors were blocked for 15 min with human or mouse TruStain blocking reagent at 37°C, then incubated with an antibody mix (Table S2) diluted in phenol red-free RPMI 1640 medium for 15min at 37°C, washed twice 2 min with phenol red-free RPMI 1640 and transferred to a glass bottom dish. 3mL phenol red-free RPMI1640 was added to the imaging dish after securing the slice with a tissue slice anchor.

Live tumour slices were imaged with a Nikon Eclipse TE equipped with a spinning disk and a temperature-controlled chamber set on 37°C and 5%CO2. Phenol red-free RPMI 1640 bubbled with carbogen (95%O2, 5%CO2) was perfused in the imaging dish at a 1mL/min rate using a double channel pump for at least 10 min prior to and during the entire recording. Areas containing myeloid cells, $CD8^+$ T cells, malignant cells and fibronectin were selected for recording, and a minimum of 2 areas were chosen per tumour slice to account for intra-tumour heterogeneity. 4D acquisition was performed with a 40-70µm z-stack, 7µm z-step on 4 channels with one time frame captured every 30 second for 30 min.

Behaviour analysis

Time-lapse recordings were projected to a single z-plane (maximum intensity projection) with the Nikon NIS-Elements software and imported in Imaris 9.1 (Oxford Instruments, Bitplane). Each recording was visualized and checked for drifting. When needed, the drifting was corrected in Imaris using the Correct 3D drift ImageJ plugin. If the fibronectin channel did not display any movement, it was used as reference channel for drift correction. If this channel couldn't be used, we instead searched for a static point in the other channels. This point was tracked through time in Imaris using the surface or spot function, masked into an additional channel and this channel was used as reference in the ImageJ plugin. Recordings were then analysed using the spot function with tracking overtime allowed, estimated diameter 10µm for myeloid and 7µm for $CD8^+$ T cells, without region growing but with background subtraction for improved signal detection. The quality threshold of the background substation was adjusted for each recording to optimise $CD8^+$ T and myeloid cell detection. The algorithm used for tracking was Autoregressive motion for myeloid and Brownian Motion for $CD8^+$ T cells, with a maximum distance set on 10µm for myeloid and 15µm for $CD8^+$ T cells and maximum gap size 3. A filter for a minimum track duration of 150 seconds was applied.

Behaviour categories

We chose to calculate the maximum displacement (MaxDis), which is the distance between a cell's initial position and the furthest it has moved from it, to split cells that migrated and cells that did not. We used a 7μm MaxDis cut-off to account for residual drifting. Cells that had MaxDis < 7μm were either wobbling or static cells. To distinguish between those two types of behaviour, we applied a trajectory length cut-off of 13μm, to account for residual drifting. Therefore cells with MaxDis < 7μm and trajectory length < 13μm were considered static, while cells with MaxDis < 7μm and trajectory length >= 13μm were considered wobbling (Figure 3C). Furthermore, we applied a >25μm cut-off on the MaxDis and a >40μm cut-off on the trajectory length to distinguish long migrating cells, while all other cells with MaxDis > 7μm were considered migrating (Figure 3C).

Behaviour data processing

All statistics for each recording were routinely exported into a folder. Using the statistical programming language R (version 4.0.4 and R studio version 1.4.1106), we have automated the aggregation of the statistics and the analysis of the different behaviours. In short, for each recording, the script computes the maximum displacement, aggregates the statistics of interest and pools the cells (myeloid or $CD8^+$ T cells) from two recordings of the same tumour together. It then aggregates all samples together, splits the static, wobbling, migrating and long migrating populations (Figure 3C), computes the percentage of the proportions for each behaviour population, extracts the statistics (proportion, trajectory length, mean speed, straightness) into individual .csv files containing easy to plot tables.

Immunohistochemistry

Tumour slices were fixed in formalin overnight at 4°C, washed in PBS and transferred to 70% ethanol until embedding. Slices were then embedded in 2% agarose and sent for paraffin embedding and longitudinal sectioning (4μm). Sections were deparaffinised twice 5min in xylene and rehydrated by successive 2min immersions in ethanol 100%, 90%, 70% and 50%, followed by 3min in dH_2O. With the exception of F4/80 and CD206 in mouse staining (proteinase K, 1 hour, room temperature), antigen retrieval was performed for 30 min in 95°C water bath with Citrate pH6 (for Ki67, cleaved-caspase 3, ccas3) or Tris-EDTA pH9 (for CD3, CD4/CD8 and CD68). Peroxidase activity was blocked by a 30min incubation in 0.6% H_2O_2 in methanol for Ki67 and ccas3 and by 10min incubation in 3% H_2O_2 in PBS. CD4/CD8 dual staining included a 40min blocking step with AffiniPure Fab Fragment Goat Anti-Mouse IgG. All sections were then further blocked with 2.5% goat serum + 2.5% bovine serum albumin for 45min and subsequently incubated with primary antibody. Detection was performed with secondary reagent or antibody and substrate as described in Table S1. Sections were counterstained in Gill's I haematoxylin or methyl green (CD4/CD8 dual staining), dehydrated with successive 3min immersions in ethanol 90%, ethanol 100% (twice), twice 5min in xylene and mounted in DPX mounting medium.

Flow cytometry

Miltenyi biotec® tumour dissociation was used according to manufacturer instructions. Briefly, 2-3 grams of tissue were cut into 2-3mm pieces using a scalpel then incubated in 4.7 ml of DMEMF12 medium and the kit enzyme mix at 37°C for 20 min with mechanical dissociation using gentleMACS™ Dissociator in gentleMACS™ C- tubes. The cell suspension was then filtered through 70μm cell strainer followed by RBC lysis.

The cell suspension was incubated with Fc blocking antibody at dilution 1:100 and fixable viability dye at dilution 1:1000 in 50μL PBS for 15 min at 4°C in the dark, then washed twice with PBS containing 2.5% BSA and 2mmol/L EDTA (fluorescence-activated cell sroting, FACS, buffer). Cells were stained with flow cytometry antibodies in FACS buffer for 20min at 4°C (described in Table S3). Cells were then washed twice with PBS containing 2.5% BSA and 2mmol/L EDTA, fixed in 2% formalin saline, washed and suspended in 200μL PBS containing 2.5% BSA and 2mmol/L EDTA. Appropriate florescence minus one (FMO) controls were used. Flow cytometry data were acquired on LSR fortessa cell analyser (BD Bioscience). Data analysis was done in FlowJo Version 10.7.3.

QUANTIFICATION AND STATISTICAL ANALYSIS

Stained sections were scanned on a 3DHISTECH Panoramic 250 digital slide scanner (3DHISTECH, Hungary) or a Hamamatsu NanoZoomer S210 Slide-Scanner. The Definiens® software (Definiens AG,

Germany) was used to quantify human Ki67, ccas3 and CD68 staining; and QuPath 0.2.3 was used to quantify human CD206 and CD3 along with mouse ccas3, Ki67, F480, CD206 and CD4/CD8. Ki67, CD3 and CD4/CD8 staining were analysed as %positive cell and all other staining as %positive area.

All statistical analysis were done with the software Graphpad Prism (San Diego, CA, version 9.0.0). The statistical tests, p values, along with n numbers are displayed in the Figure legends.